Development of a Thermoelectric Harvesting Unit to Retrofit a Vortex Tube for Remote Monitoring Applications

Mariana Ramos

Mestrado em Engenharia Física

Departamento de Física e Astronomia

2023

Orientador

Prof. Dr. André Pereira, Faculdade de Ciências da Universidade do Porto

MSc

U.PORTO

FACULDADE DE CIÊNCIAS
UNIVERSIDADE DO PORTO

MSc

Sworn Statement

I, Mariana Silva Barbosa Castro Ramos, enrolled in the Master Degree in Engineering Physics at the Faculty of Sciences of the University of Porto hereby declare, in accordance with the provisions of paragraph a) of Article 14 of the Code of Ethical Conduct of the University of Porto, that the content of this internship report reflects perspectives, research work and my own interpretations at the time of its submission.

By submitting this internship report, I also declare that it contains the results of my own research work and contributions that have not been previously submitted to this or any other institution.

I further declare that all references to other authors fully comply with the rules of attribution and are referenced in the text by citation and identified in the bibliographic references section. This internship report does not include any content whose reproduction is protected by copyright laws.

I am aware that the practice of plagiarism and self-plagiarism constitute a form of academic offense.

Mariana Silva Barbosa Castro Ramos

Porto, June 29th, 2023

“ Accident is the first building block of evolution. ”

Dr. Amelia Brand in *Interstellar*, written by Jonathan and Christopher Nolan

Acknowledgements

I would like to express my heartfelt gratitude to my supervisors, Professor André Pereira and Cátia Rodrigues, for giving me the opportunity to work at inanoEnergy and participate in the innovative and exciting projects the company is involved in. Their belief in my abilities and trust in my decision-making empowered me to explore new ideas and their support and guidance were imperative for the success of this internship.

I want to extend my gratitude to Professor João Ventura and João Magalhães for their willingness to lend a helping hand and always being ready to discuss and share new ideas, making the work environment educational and stimulating. I also want to thank all the IFIMUP members for their invaluable support, in particular Dr. Ana Pires for her patience, guidance and unwavering assistance, even when I wasn't so patient myself.

Additionally, I want to thank the NFP group at INMA, especially Professors Maria Pilar and Reyes Mallada, and my friend Isabel Sanches, for the warm reception and for going out of their way to ensure I had the resources and guidance needed to accomplish my tasks. I would also like to show my gratitude to the MinoS group at URV, particularly Professor Eduard Llobet as well as Xavi Blanch for their warm reception, their assistance and for sharing their expertise.

I am deeply indebted to my dear friends Joana Teixeira, Ana Melo, Cristiana Sousa, Diana Silva, Hugo Sousa and Ricardo Lagoa, whose friendship, support and encouragement kept me motivated and determined, and who always brought laughter to the most trying and stressful situations.

Last but not least, I must thank my parents for the sacrifices they have made to provide me with the opportunities that got me here, for always being by my side no matter what, for never putting pressure on me, and for their love, support and unwavering belief in me. I must also thank my cousins and especially my sister for the fun-filled moments we share together, from joyful gatherings to lively board game sessions, their love and encouragement have given me the strength to overcome all obstacles.

To all those who have contributed to the successful completion of this internship,

Thank you!

UNIVERSIDADE DO PORTO

Abstract

Faculdade de Ciências da Universidade do Porto
Departamento de Física e Astronomia

MSc. Engineering Physics

Development of a Thermoelectric Harvesting Unit to Retrofit a Vortex Tube for Remote Monitoring Applications

by Mariana RAMOS

The rapid development of the Internet of Things (IoT) has led to a high demand for self-powered, sustainable devices, as a means to replace batteries and reduce the need for wired connectors. For this reason, the phenomenon of converting ambient energy into electrical energy, known as energy harvesting, has been extensively investigated as an alternative to typical energy sources. Thermoelectric generators (TEGs) have received special attention for their ability to convert otherwise wasted thermal energy into useful electric energy, making them a clean and sustainable energy source.

This work's goal is to develop an energy harvesting unit (EHU) that can be retrofitted on a vortex tube to take advantage of the high temperatures it generates, and be integrated in a gas distribution network to power a processing unit (PU) for in-situ monitoring.

In the first part of this work, the EHU consists of the assembly of commercial TEGs on a geometry that can be placed around the vortex tube and are topped by metallic heatsinks. For that, the shape and material of the geometry were optimized as well as the heatsink's dimensions through numerical simulations. Three different prototypes were made and tested on the vortex tube. The highest outputs were produced by a 3D printed geometry made of polylactic acid with $10 \times 10\,\mathrm{mm}^2$ TEGs, which generates a maximum output power of 37.3 mW (460 mV of voltage and 80.5 mA of electric current) for a TEG temperature gradient of 16.9 °C.

In the second part, flexible screen-printed radial TEGs that can be placed around the tube were optimized. Numerical simulations were performed to optimize their design, and since the device's thickness is difficult to control through screen-printing, the impact

of printing 1 to 4 layers was studied, as well as the influence of two different thermal treatments. It was concluded that each layer increases the thickness by about 50 μm and slightly increases the surface roughness. The morphological, crystalline and transport properties of the thermoelectric ink are not affected by the number of printed layers or by the thermal treatments. Its Sebeeck coefficient and electric conductivity average -97 μV/K and 100 S/m, respectively, which corresponds to a power factor of 0.93 $\mu W/(K^2 m)$. Thermogravimetric analysis shows that the ink can endure temperatures up to 500 °C and therefore wouldn't deteriorate for the intended application. Preliminary tests of the mechanical stability indicate that the thickness increases the ink's brittleness and worsens its flexibility.

Additionally, the radial TEGs with 10 thermoelectric stripes connected in series were printed, also with 1 to 4 layers of the thermoelectric ink and underwent the two thermal treatments. It was verified that under the same measurement conditions, the devices' temperature gradient was roughly the same, and therefore so was their output voltage. However, because their internal resistance decreases with the ink's thickness, the number of printed layers increases the output power. A proof of concept device made of 20 radial TEGs was printed with 1 layer and tested on the vortex tube. A maximum output of 100.15 nW was measured, which allows us to predict that if a device was produced with the maximum number of TEGs that can fit on the tube, outputs of 1.10 μW could be generated, and this value could be further increased by printing more layers of the thermoelectric ink. Although this approach generates less energy than the first, these devices are less bulky and easier to manufacture and employ.

Finally, a self-power sensor IoT system was built, using the first prototypes developed to power a PU capable of feeding a sensor, reading its signal and sending it wirelessly. It was confirmed that the devices generate enough energy to power the PU and allow it to continuously feed a graphene sensor with a voltage of 3.5 V, correctly read the sensor's voltage drop and send the read data at minimum rate of $1.5\,s^{-1}$.

UNIVERSIDADE DO PORTO

Resumo

Faculdade de Ciências da Universidade do Porto
Departamento de Física e Astronomia

Mestrado em Engenharia Física

Desenvolvimento de uma Unidade de Colheita de Energia Termoelétrica para Instalação num Tubo Vórtex para Aplicações de Monitorização Remota

por Mariana RAMOS

O rápido desenvolvimento da Internet das Coisas (IoT) levou a uma alta procura por dispositivos autoalimentados e sustentáveis, como forma de substituir as baterias e reduzir a necessidade de conectores com fio. Por esta razão, o fenómeno de conversão de energia ambiente em energia elétrica, conhecido como colheita de energia, tem sido investigado extensivamente como alternativa às típicas fontes de energia. Geradores termoelétricos (TEGs) têm recebido atenção pela sua capacidade em converter calor de outra forma desperdiçado em energia elétrica útil, tornando-os uma fonte de energia limpa e sustentável.

O objetivo deste trabalho é desenvolver uma unidade de colheita de energia (EHU) que possa ser instalada num tubo vórtex para tirar vantagem das altas temperaturas que este gera, e ser integrada numa rede de distribuição de gás para alimentar uma unidade de processamento (PU) para monitorização no local.

Na primeira parte deste trabalho, a EHU consiste na montagem de TEGs comerciais em cima de uma geometria que pode ser colocada ao redor do tubo vórtex e são encimados por dissipadores de calor metálicos. Para isso, a forma e material da geometria foram otimizados, assim como as dimensões dos dissipadores de calor, por simulações numéricas. Por fim, três protótipos distintos foram produzidos e testados no tubo vórtex. Os melhores resultados foram produzidos por uma geometria impressa em 3D feita de ácido polilático com TEGs de $10 \times 10\,\mathrm{mm}^2$, que gera uma potência máxima de 37.3 mW (460 mV de tensão e 80.5 mA de corrente) para um gradiente de temperatura dos TEGs de 16.9 °C.

Na segunda parte, TEGs flexíveis e radiais foram fabricados e otimizados usando screen-printing para serem colocados à volta do tubo. Simulações numéricas foram efetuadas para otimizar o seu design, e uma vez que a espessura dos dispositivos é difícil de controlar por screen-printig, o impacto de imprimir 1 a 4 camadas foi estudado, bem como a influência de dois tratamentos térmicos diferentes. Foi concluído que cada camada aumenta a espessura por cerca de 50 µm e aumenta ligeiramente a rugosidade da superfície. As propriedades morfológicas, cristalinas e de transporte da tinta termoelétrica não são afetadas pelo número de camadas impressas ou pelo tratamento térmico. O seu coeficiente de Sebeeck e condutividade elétrica são em média -97 µV/K e 100 S/m, respetivamente, o que corresponde a um fator de potência de 0.93 $\mu W/(K^2 m)$. Análises termogravimétricas mostram que a tinta consegue aguentar temperaturas até 500 °C e por isso não seria degradada na aplicação pretendida. Testes preliminares das propriedades mecânicas indicam que o aumento da espessura aumenta a fragilidade da tinta e piora a sua flexibilidade.

Adicionalmente, TEGs radiais com 10 listras termoelétricas conectadas em série foram imprimidos, também com 1 a 4 camadas da tinta termoelétrica e sofreram os dois tratamentos térmicos. Foi verificado que nas mesmas condições de medição, o gradiente de temperatura dos dispositivos era aproximadamente o mesmo, e por isso a sua tensão também. Contudo, como a sua resistência interna diminui com a espessura da tinta, o número de camadas impressas aumenta a potência gerada. Um dispositivo de prova de conceito feito de 20 TEGs radiais foi imprimido com 1 camada e testado no tubo vórtex. Uma potência máxima de 100.15 nW foi medida, o que nos permite prever que se um dispositivo fosse produzido com o número máximo de TEGs que cabem no tubo, potências de 1.10 µW poderiam ser geradas. Este valor poderia ser ainda aumentado pela impressão de mais camadas da tinta termoelétrica. Apesar desta abordagem gerar menos energia que a primeira, estes dispositivos são menos volumosos e mais fácies de produzir a aplicar.

Finalmente, um sistema IoT de sensor de auto-alimentação foi desenvolvido, utilizando os primeiros protótipos produzidos para alimentar uma PU capaz de alimentar um sensor, ler o seu sinal e enviá-lo sem fios. Foi confirmado que os dispositivos geram energia suficiente para alimentar a PU e permitir que esta alimente continuamente um sensor de grafeno com uma tensão de 3.5 V, ler corretamente a queda de tensão no sensor e enviar os dados coletados a uma taxa mínima de 1.5 s^{-1}.

Contents

List of Figures

List of Tables

Symbols

$\varnothing$	Diameter	mm
η	Efficiency	
σ	Electric Conductivity	S/m
I	Electric Current	A
ZT	Figure-of-merit	
$\dot{q}$	Heating/Cooling Rate	K/s
Δz	Height Variation	μm
π	Peltier Coefficient	J/C
P	Power	W
PF	Power Factor	$W/(K^2m)$
R	Resistance	Ω
S	Seebeck Coefficient	V/K
T	Temperature	°C
ΔT	Temperature Gradient	°C
k	Thermal Conductivity	W/(Km)
V	Voltage	V
ΔV	Voltage Difference	V

Glossary

CF	**C**old **F**raction
DTG	**D**ifferential **T**hermo**g**ravimetric Analysis
EHU	**E**nergy **H**arvesting **U**nit
FTIR	**F**ourier **T**ransform **I**nfra**r**ed
IFIMUP	**I**nstituto de **F**ísica de **M**ateriais Avançados, Nanotecnologia e Fotónica da **U**niversidade do **P**orto
INMA	**I**nstituto de **N**anociencia y **M**ateriales de **A**ragón
IoT	**I**nternet **o**f **T**hings
PLA	**P**oly**l**actic **A**cid
PVA	**P**oly**v**inyl **A**lcohol
PU	**P**rocessing **U**nit
SCFM	**S**tandard **C**ubic **F**eet per **M**inute
SEM	**S**canning **E**lectron **M**icroscopy
TEG	**T**hermo**e**lectric **G**enerator
TRL	**T**echnology **R**eadiness **L**evel
TGA	**T**hermo**g**ravimetric **A**nalysis
URV	**U**niversitat **R**ovira i **V**irgili

Chapter 1

Introduction

1.1 Motivation

The Internet of Things (IoT) consists of a system of ”smart devices” that are interrelated and can connect and exchange data with each other over communications networks, without the requirement for human-to-human or human-to-computer interaction [1]. This is only feasible with the availability of robust wireless internet technologies such as 5G and future 6G networks [2, 3]. IoT has the potential to make our lives easier by taking everyday devices (like a coffee machine, a watch or even a pet feeder) and allowing us to remotely control them, access data and know how they are operating [4]. IoT is a crucial component of smart cities, making it possible to collect and analyze data from various sources such as sensors, devices, and citizen inputs, which allows a better monitorization and management of energy consumption, traffic flow and public safety, improving the residents’ quality of life [5, 6]. Furthermore, IoT has significant implications for Industry 4.0, also known as the Fourth Industrial Revolution, which leverages advanced digital technologies, automation, and connectivity to transform manufacturing and industrial processes [7]. The IoT facilitates a connectivity that can increase efficiency, productivity, and flexibility in manufacturing operations [8].

For that, the devices need processors, sensors and communication hardware to send, receive and act on the data they collect, which require a power source [9]. The most used power sources are wired connectors, which limit mobility, and batteries, which are costly, need frequent recharging or replacement and have a finite lifetime [10]. With the rapid development of IoT, the number of IoT devices has increased significantly in recent years [see Figure 1.1(a)], with an estimated 50.1 billion devices in use by 2020 [11]. This led to a high demand for low-cost, self-powered devices, which require the development of innovative energy-efficient technologies [12]. In recent years, the phenomena of conversion of ambient energy into electrical energy, also known as energy harvesting [13] [Figure 1.1(b)], gained high relevance, such as piezoelectricity (electric polarization induced by the application of mechanical stress, leading to positive and negative charge centers appearing on the opposite surface of the materials [14]), triboelectricity (two highly insulating materials become electrically charged when they come into contact and are then separated [15]), magnetic induction (electrical voltage induced by a time-varying magnetic field, in which the electric voltage level depends on the magnetic permeability of the surrounding material [16]) and thermoelectricity (conversion of thermal energy from a temperature gradient into electrical energy [17]).

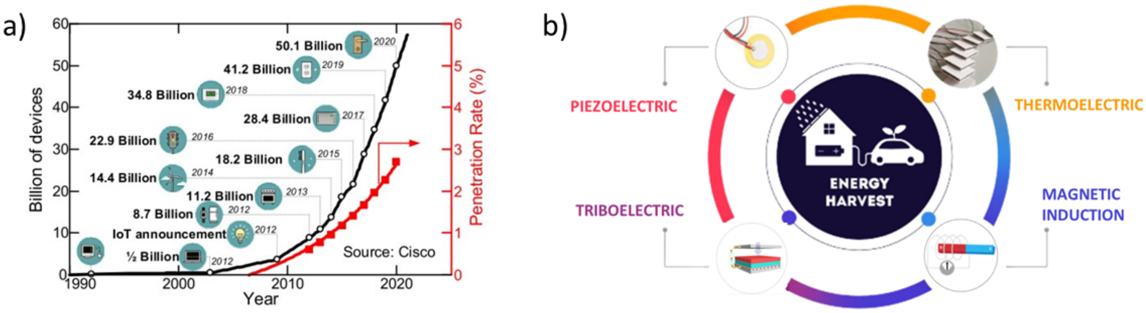

FIGURE 1.1: (a) Number of IoT devices and their percentage market penetration over the years [11]. (b) Types of energy harvesting. Adapted from Ref. [18].

Thermal energy presents the highest losses because it is the hardest to conserve [11]. M. Papapetrou *et al.* [19] estimate that the European Union has a total waste heat potential of 300 TWh/year, with around 66% of it being temperatures below 200 °C and 25% being between 200 and 500 °C. In China, waste heat corresponds to 42% of the total primary energy inputs, where most comes from the electricity generation and the industry sectors (see Figure 1.2) and 66% of waste heat corresponds to temperatures below 100 °C [20].

In light of this, thermoelectric generators (TEGs) gain relevance due to their ability of directly converting waste heat into useful electrical energy, being among the cleanest sustainable energy sources [17].

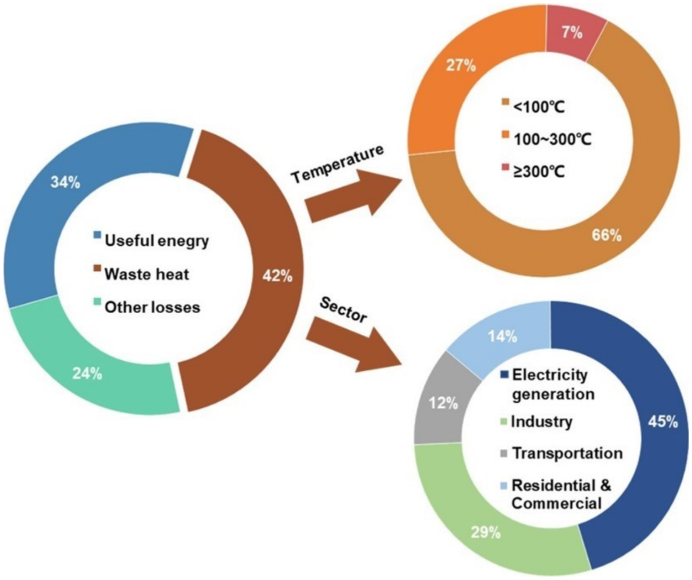

FIGURE 1.2: China's waste heat in different sectors and at different temperatures in 2018 [20].

1.2 Thermoelectric Effect

The thermoelectric effect is divided into three effects: the Seebeck, Peltier and Thomson effects.

The Seebeck effect was the first to be discovered and is the conversion of a material's thermal gradient into an electric voltage, as shown in Figure 1.3(a). This phenomenon is due to the thermal gradient creating an energy gradient in the conduction band, that is, the charge carriers closer to the hot side are more energetic and therefore tend to diffuse to the cold side, leading to an uneven distribution of charge and creating a potential difference [21]. This effect is characterized by the Seebeck coefficient, S, defined as [22]:

$$S = -\lim_{\Delta T \to 0} \frac{\Delta V}{\Delta T}, \tag{1.1}$$

where ΔV is the resulting electric potential difference and ΔT the temperature gradient between the two ends of the material. Note that n-type materials have a majority of electrons as charge carriers, having negative S in accordance with Equation 1.1, while p-type materials have a majority of holes, having positive S [21]. This signal corresponds to the relative directions of the temperature gradient and the electromotive force generated [23].

As opposed to the Seebeck effect, the Peltier effect is the generation of a temperature gradient from an electric current, as illustrated in Figure 1.3(b). The Peltier coefficient is given by $\pi = \dot{q}/I$, where $\dot{q}$ is the heating/cooling rate and I the electric current flowing through the material. Lastly, the Thomson effect acknowledges the relation between the Seebeck and Peltier effects ($\pi = S.T$) and combines them, reversibly heating or cooling when an electric current and a temperature gradient are present [22].

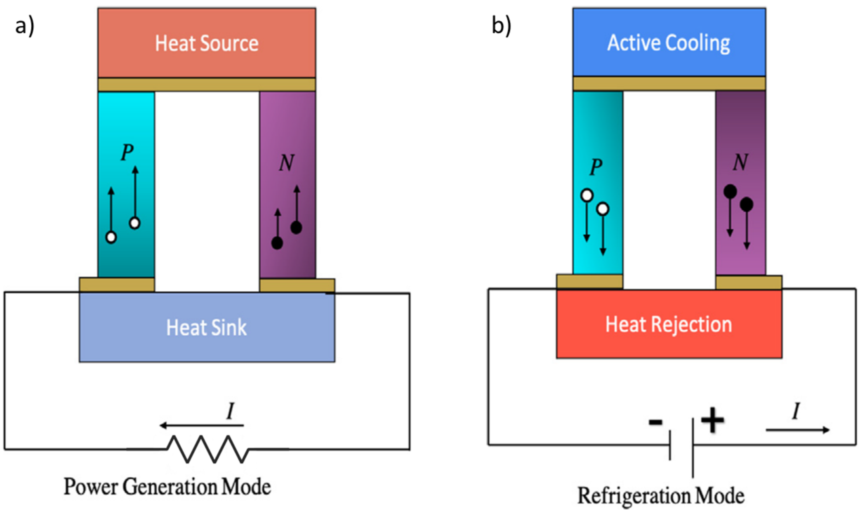

FIGURE 1.3: Schematic illustration of (a) the Seebeck effect for power generation and (b) the Peltier effect for active cooling [21].

These three thermoelectric properties enable the development of TEGs, devices capable of cooling or heating from an electric current or generating electrical power from a temperature gradient.

1.2.1 Thermoelectric Figure-of-Merit

The performances of different thermoelectric materials can be compared using the dimensionless figure-of-merit, ZT, which relates the material's Seebeck coefficient (S), its electrical conductivity (σ), its absolute temperature (T) and its thermal conductivity (k) [24]:

$$ZT = \frac{S^2 \sigma T}{k}. \tag{1.2}$$

From Equation 1.2, a high-quality thermoelectric material must have high S, as well as high σ and low k. However, these three transport parameters are interrelated and depend on material features like the band structure, carrier concentration, among others [17]. Nowadays, inorganic thermoelectric materials like bismuth telluride (Bi_2Te_3), lead telluride (PbTe) and stannic selenide (SnSe) present ZT values above unity [24].

The product of the square of the Seebeck coefficient with the electrical conductivity is known as the power factor (PF) and it can also be used to compare the performance of thermoelectric materials, disregarding k [17]:

$$PF = S^2\sigma. \tag{1.3}$$

The ratio of the power a TEG generates to the heat it absorbs is known as its power conversion efficiency (η) and is given by [25]:

$$\eta = \frac{\Delta T}{T_h}\frac{\sqrt{1+ZT}-1}{\sqrt{1+ZT}+T_c/T_h}, \tag{1.4}$$

where T_h ans T_c are the temperatures on the hot and cold sides, respectively and ΔT the temperature gradient.

For large ZT values, η tends to $\frac{\Delta T}{T_h}$, that corresponds to the Carnot efficiency, which limits the maximum efficiency of a TEG [26].

1.3 Applications

In recent years, TEGs have received a lot of attention and many articles have been published with various applications of thermoelectricity for the recovery of waste heat. Since TEGs are relatively easy to install in extreme environments and allow wireless power transfer (WPT), this technology is already being used for the generation of energy and low-power supply in a wide range of sectors [27].

One example of the application of TEGs for waste heat recovery is the assembly of commercial TEGs around a composting system tube developed by R. S. Rodrigues *et al.* [28], where heatsinks were used to maximize the thermal gradient, as represented in Figure 1.4. In that study, a temperature gradient of 20 °C was achieved, which allowed the generation of a maximum power density of 175 mW/m^2 for a load resistance of 500 Ω and the system was used to power a humidity and temperature sensor with 225 μW/h for 12 min [28].

A similar strategy was employed by H. Khalil *et al.* [29] to recover waste heat on a vertical chimney using TEGs topped with heatsinks and they confirmed that the use of heatsinks greatly improves the thermal gradient, and therefore the outputs.

A different application was carried out by P. Alegria *et al.* [30] where geothermal energy from shallow hot dry rock fields is taken advantage of to generate thermoelectricity. In this case, commercial TEGs are placed between a thermosiphon that is inserted into a shallow hot dry rock field, and hestasinks connected to four heat pipes, as shown in

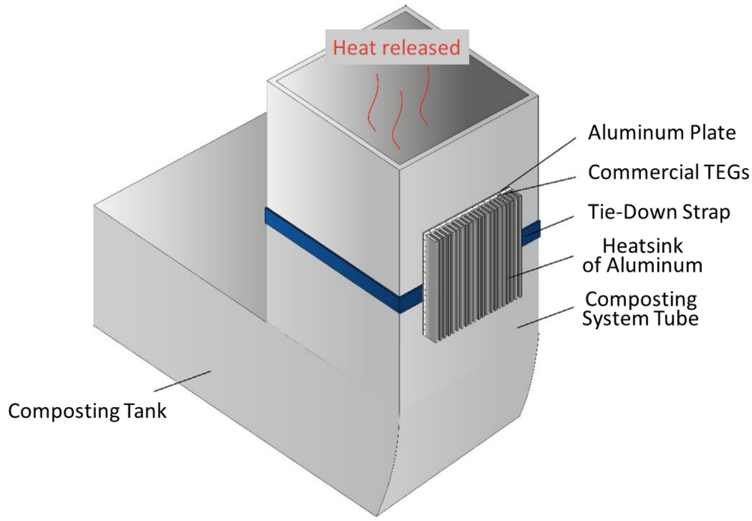

FIGURE 1.4: Schematic diagram of the heat recovery system installed at the composting conduct. Adapted from Ref. [28].

Figure 1.5(a). Using 10 TEGs, they were able to generate 16.78 W for a TEG temperature gradient of 94.7 °C.

K. T. Park *et al.* [31] developed a flexible thermoelectric bracelet that consists of thirty pairs of n- and p-doped carbon nanotube ink which was printed on a circular flexible cable [see Figure 1.5(b)]. By wearing the bracelet, a gradient of 4 °C was created by the skin and the surrounding ambient and an output voltage of 91 mV was measured for a bracelet internal resistance of 1006 Ω.

In the automotive industry, since the exhaust gas system and the radiator waste 65% to 70% of the internal combustion engine energy input in the form of heat, the use of TEGs could lead to a gain in efficiency and a reduction in fuel consumption, as discussed by N. V. Burnete *et al.* [32].

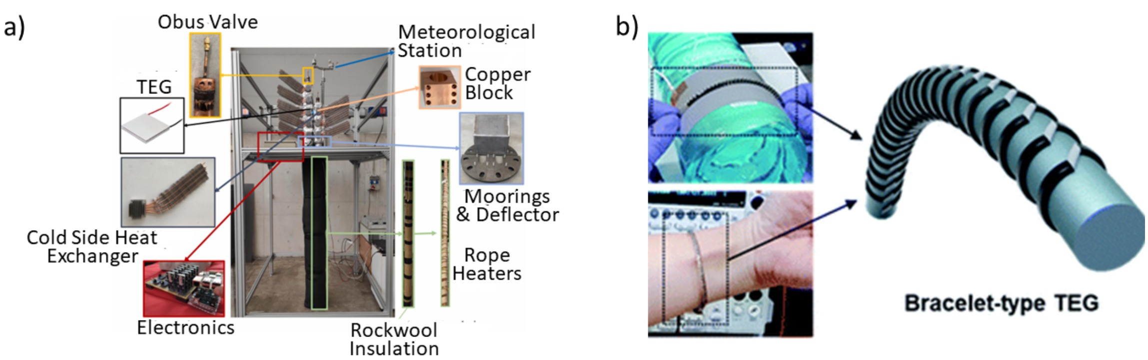

FIGURE 1.5: (a) Geothermal TEG to install at shallow hot dry rock fields. Adapted from Ref. [30]. (b) Bracelet-type TEG which can harvest waste heat on any curved surface [31].

The appeal of TEG's applications lies not only in being among the cleanest sustainable energy sources, but also because they are solid-state operation devices that do not generate toxic waste, have wide scalability, and the absence of moving parts or chemical reactions ensure a long-life span of reliable, maintenance-free operation [17].

In recent years, materials at the nanoscale have been explored as a way of reducing the thermal conductivity by including a lot of grain boundaries and other dispersion centers, which diffuse photons but do not scatter electrons [21]. In this way, thermal conductivity can be reduced without reducing electrical conductivity, therefore increasing the material's figure-of-merit and improving the device's output.

With the constant scientific advances, it is to be expected that thermoelectric devices will continue to improve, leading to the emergence of more applications, with devices capable to satisfy the energetic demand caused by the increasing number of IoT devices.

1.4 Objectives

This academic internship was carried out at inanoEnergy and is integrated in the ATTRACT R&D&I PiPe4.0 and the MSCA-RISE SENSOFT projects of high level of Technology Readiness Level (TRL5-7). The internship aim is to develop an energy harvesting unit (EHU) to power a processing unit (PU) for in-situ monitoring in a particular place in a fuel gas distribution network.

A gas distribution network must deliver a constant pressure to the users, independently of the network feed pressure and the delivery flow rate, which is achieved by a pressure reducer unit. The pressure reducer unit causes a difference in pressure between its two sides, which can be used to cause a part of the gas to flow through a vortex tube, which is a mechanical device with no moving parts that separates a high-pressure inlet gas stream into two streams of lower pressure, one hot and the other cold [33].

When the compressed gas enters the vortex tube, it passes through a nozzle in the vortex generation chamber, like the one in Figure 1.6(a), that sets the gas into a vortex motion and makes it enter tangentially into the hot end tube [34]. The high-speed stream heats up as it spins along the periphery of the hot end tube, and when it reaches the control valve a part of the gas exits the tube (the control valve can be adjusted to control the percentage of gas that exits). The percentage of gas that doesn't exit the tube is called cold fraction (CF) and is forced to slow down and counter-flow through the center of the high-speed hot stream, as illustrated in Figure 1.6(b). As it spins back through the hot tube, this second vortex gives up energy to the first vortex in the form of heat, exiting the other end of the tube [35, 36]. The energy separation is very complex and various theories have been formulated to try to explain it [33, 36].

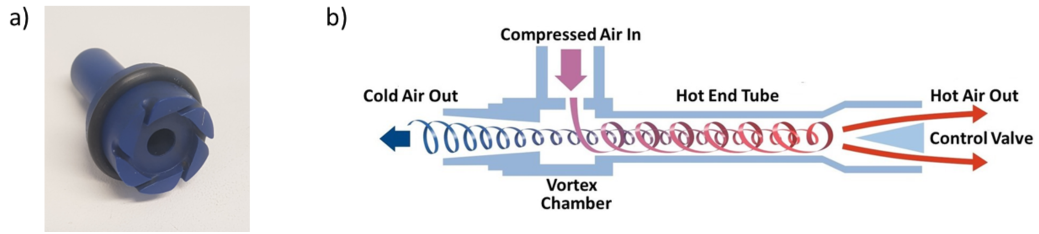

Figure 1.6: (a) Vortex generator. (b) Schematic diagram of vortex tube [35].

By integrating the vortex tube into the distribution network, thermoelectricity can be used to take advantage of the temperature gradient created between the hot end tube and the surrounding environment, and generate energy to power the PU for in-situ monitoring.

Considering the advances made in the field of thermoelectrics over the recent years, this work seeks to create a EHU that can be retrofitted on the hot end tube of the vortex tube and thus focuses on two approaches: the first using commercial TEGs and the second using flexible screen-printed TEGs.

In the first approach, commercial TEGs of different dimensions were assembled on two different geometries and the impact of heatsinks on the thermal gradient, and consequently the device's output, was studied towards a fast market entry.

In the second approach, a more exploratory task was carried out by using radial 2D printed TEGs with different thicknesses and thermal treatments. Their transport and morphological properties, as well as their flexibility, were analysed and compared.

Additionally, tests were made where the prototypes powered a processing unit made by inanoEnergy that reads gas sensor information and sends data throughout a wireless communication protocol, as represented in Figure 1.7.

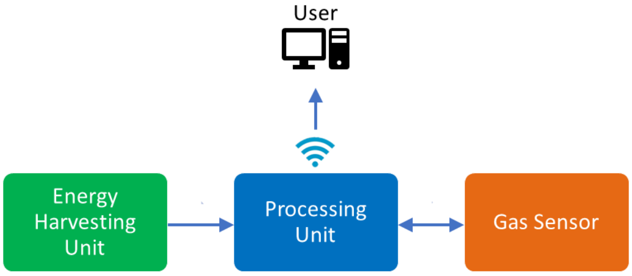

Figure 1.7: Schematic diagram of the energy harvesting system.

Chapter 2

Development of Functional Energy Harvesting Unit Using Commercial TEGs

This chapter focused on developing an EHU made of commercial TEGs that can be retrofitted on the surface of the hot end tube of the vortex tube.

For that purpose, this chapter begins with a study of the thermal outputs of the hot tube in order to evaluate the temperature distribution along the tube, as well as its stability, and determine if it is suitable to be used for this application.

In the second section of this chapter, *COMSOL* simulations were used to optimize the design of the EHU. Two geometries were considered and the influence of their width on the TEG's temperature gradient was studied, as were the dimensions of heatsinks.

Three prototypes were made and their outputs were measured as a function of the TEG's thermal gradient and as a function of a load resistance, in order to determine the maximum power and internal resistance of each prototype and determine which performs the best.

2.1 Thermal Outputs of Vortex Tube

In this work, the vortex tube Model 208 from the company Vortec was used [37]. This vortex tube requires a minimum air flow of 11 SCFM, however, when testing it wasn't possible to achieve such a high flow, so the maximum temperatures generated by the tube weren't as high as the datasheet predicted. Since the hot air temperature is higher for a higher cold fraction (CF), all tests were performed using CF = 85 %.

Given that the EHU is to be retrofitted on the hot end tube, it is necessary to study the temperature distribution along the tube's surface and its stability. For that purpose, the surface temperature of the hot tube was measured at different positions, for a inlet pressure of 4 bar, and the results are presented in Figure 2.1(a). As expected, the temperature is lowest near the inlet and increases toward the hot air outlet, where it reaches the maximum temperature of 72.2 °C. The average temperature of the surface of the tube is 56.4 °C. The temperature was also measured continuously to study the thermal stability. The results of the measurement made near the outlet of the tube are shown in Figure 2.1(b) and it is seen that the temperature stabilizes after about 2 minutes and remains relatively stable. This also applies for the entire length of the hot end tube.

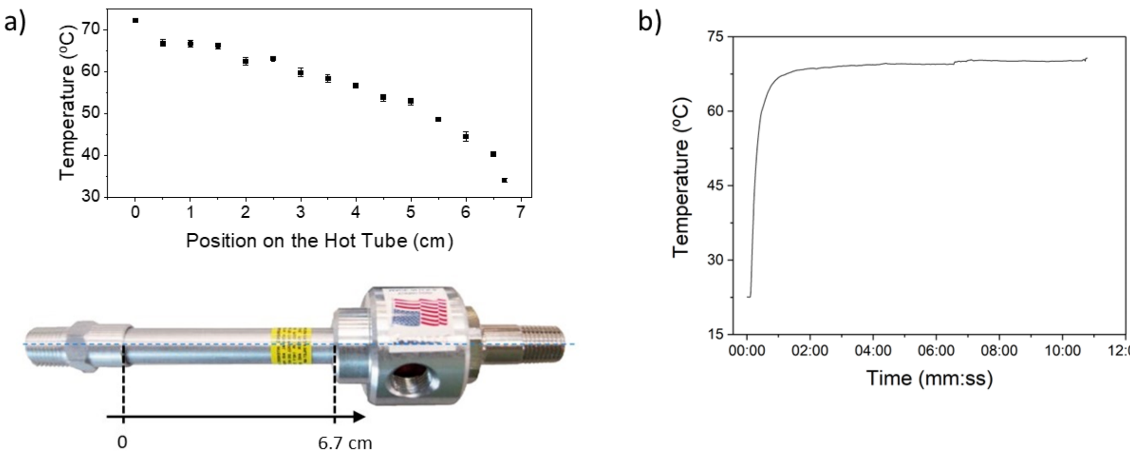

FIGURE 2.1: (a) Surface temperature along the hot tube, and (b) thermal stability of the surface of the vortex tube, for a inlet gas pressure of 4 bar and CF = 85 %.

It outcomes that under these conditions, the vortex tube generates high temperatures on the surface of the hot end tube that are constant over time, making it a desirable device to implement the EHU.

2.2 Numerical Simulations

To optimize the design required for the EHU and determine the behavior of the temperature gradient created, heat transfer simulations were performed on *COMSOL Multiphysics 5.5*.

Two geometries were studied, both consisting of two halves of a material that can be installed on the surface of the hot end tube of the vortex tube. The TEGs and heatsinks are assembled on top of that geometry. The first geometry is made of polylactic acid (PLA) and has open gaps between the surfaces of the hot tube and the TEGs, which are filled with thermal grease to improve thermal conductivity. The second geometry is made of solid aluminium (Al) and, due to its high thermal conductivity, has no gaps.

The two geometries were introduced at the *COMSOL* platform as shown in Figure 2.2, and the influence of the wall thickness of the geometry was studied, as well as the use of heatsinks and their height and width, and the temperature gradient time dependency.

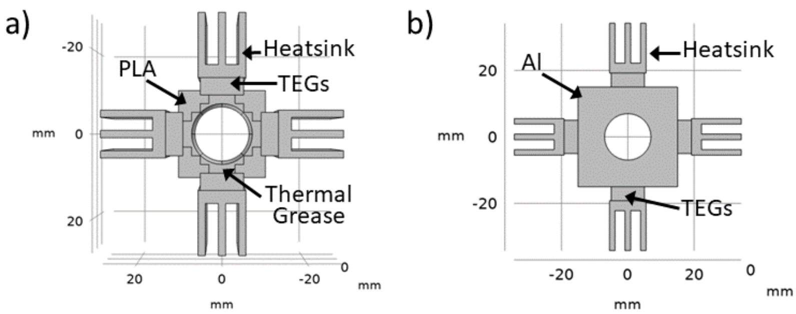

FIGURE 2.2: Schematic illustration of the front view of (a) the PLA and (b) the Al geometries.

The simulations were performed using *COMSOL* module *Heat Transfer in Solids* and considered heat flux between all materials and surface-to-ambience radiation losses. The hot tube's surface was set to a constant temperature of 60 °C, the TEGs' dimensions were set to $10\times10\times4.2\,mm^3$, and the thermoelectric material chosen was pure Bi_2Te_3 from the *COMSOL* library. The heatsinks are made of Al, also from *COMSOL* library, and their fins have a width of 1.7 mm. In order to improve thermal conductivity, thermal grease was added to the surfaces of the TEGs as a boundary material.

The results of the simulations are presented in Figure 2.3.

In regards to the heatsink's dimensions, the simulations for its height and width were performed individually, and the wall thickness of the geometry was fixed at 25 mm for both geometries. Its height ranged from 0 to 50 mm while its width was fixed at 11 mm, and its width ranged from 0 to 30 mm while the height was fixed at 15 mm. The graphs from Figure 2.3(a),(b) show that the heatsinks significantly improve the thermal gradient and that the gradient increases with heatsink dimensions. However, when choosing the heatsink dimensions, its weight, available fitting space and cost of manufacture should be taken into account.

The wall thickness of the material that is in contact with the hot tube ranged between 15 and 50 mm, for both geometries. The heatsink's height and width were constant at

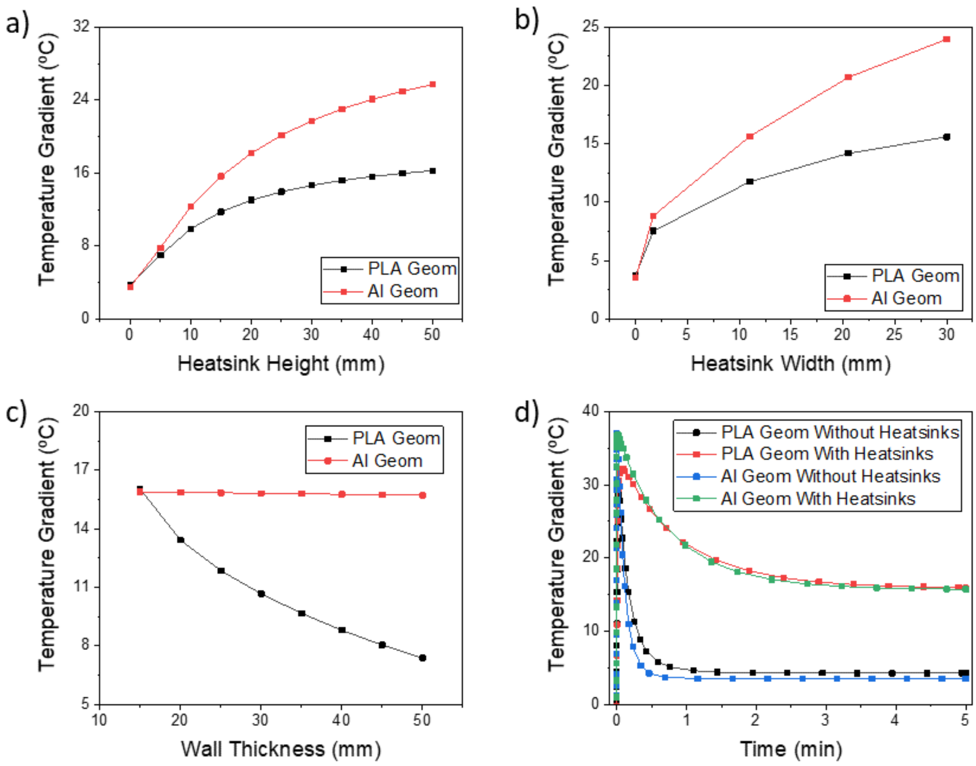

FIGURE 2.3: Simulation results for the influence of (a) the heatsink's height and (b) width, and (c) the thickness of the base material on the TEG's temperature gradient; and (d) the temperature gradient time dependency for both geometries, with and without heatsinks.

15 mm and 11 mm, respectively. Figure 2.3(c) shows that the wall thickness has very little impact on the Al geometry, but significantly reduces the TEG's thermal gradient on the PLA geometry as it increases. These results are due to Al's high thermal conductivity and PLA's poor thermal conductivity. The results imply that for thinner walls, the performance of both geometries is similar and, since PLA is cheaper and easier to manufacture, the PLA geometry would be the most appropriate. However, if thicker walls are required for integrity purposes, the Al geometry is the best choice.

Finally, the stability of the TEG's temperature gradient was studied by performing time dependent simulations for a time range of 5 minutes. These simulations were performed with and without the heatsinks. The wall thickness of the base material was fixed at 25 mm and, when used, the heatsink's height and width were constant at 15 mm and 11 mm, respectively. From Figure 2.3(d) it is concluded that, for these conditions, the two geometries present similar behaviors, both with and without heatsinks. When no heatsinks are used, the thermal gradient stabilizes quickly, but its value is low. In contrast, when heatsinks are used, the thermal gradient takes a few more minutes to stabilize, but the gradient is much higher, as seen in Figure 2.4. However, it is important to notice that these simulations assume that the surface temperature of the hot tube is already stable when the measurements begin, which will not be the case in real life and, therefore, the TEG's temperature gradient might take a little longer to stabilize.

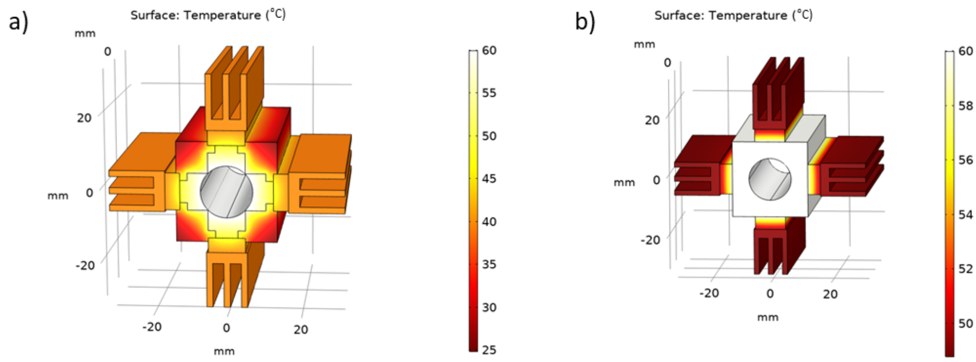

FIGURE 2.4: Simulation results for the temperature distribution on (a) the PLA and (b) the Al geometries with heatsinks after stabilizing.

2.3 Experimental Apparatus

Considering the results from the previous section, the PLA geometry should have a wall thickness as small as possible but the Al geometry can be as big as necessary. Therefore, given the dimensions of the hot tube ($\varnothing = 12.72$ mm), TEGs of $10\times10\times4.2\,\text{mm}^3$ were used on the PLA geometry. However, since Al has high thermal conductivity, its dimensions can be increased to also fit $20\times20\times3.5\,\text{mm}^3$ TEGs, which are expected to perform better.

Hence, considering the area required to assemble the TEGs and secure the prototypes on the vortex tube, the PLA geometry has a wall thickness of 15 mm and can accommodate six $10\times10\,\text{mm}^2$ TEGs on each side, for a total of twenty-four TEGs. As for the Al geometry, for a wall thickness of 30 mm, it can fit eight $10\times10\,\text{mm}^2$ TEGs on each side, for a total of thirty-two TEGs. Alternatively, for a wall thickness of 40 mm, it can accommodate three $20\times20\,\text{mm}^2$ TEGs on each side, making a total of twelve TEGs.

Figure 2.5 shows one half of the assembled prototypes, without heatsinks. On the Al geometries, there is thermal grease between the TEGs and the Al and, in all prototypes, the TEGs are fixed with silicone.

According to the results of Section 2.2, the heatsinks should be as big as possible to obtain maximum thermal gradients. However, considering the available space and the

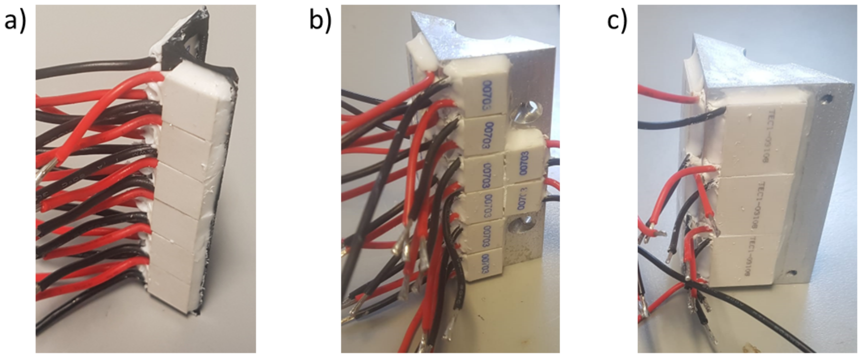

Figure 2.5: Assembled prototypes without heatsinks: (a) 10×10 mm^2 TEGs on PLA geometry; (b) 10×10 mm^2 TEGs on AL geometry; and (c) 20×20 mm^2 on Al geometry.

heatsinks that the company already had, the heatsinks used had 15 mm of height, fins 1.7 mm wide, and width of 15 mm for the PLA geometry and 30 mm for the Al geometries.

To secure the heatsinks on top of the TEGs, PLA clamps like the one in Figure 2.6(a) were designed. The clamps are screwed together in pairs and each pair of clamps secures two heatsinks. The clamps have fins that fit into the heatsink to prevent it from moving from side to side. To improve thermal conductivity, thermal grease was added between the TEG's surface and the heatsinks. Figure 2.6(b),(c) shows the prototype made of 20×20 mm^2 TEGs on the Al geometry assembled on the vortex tube with heatsinks.

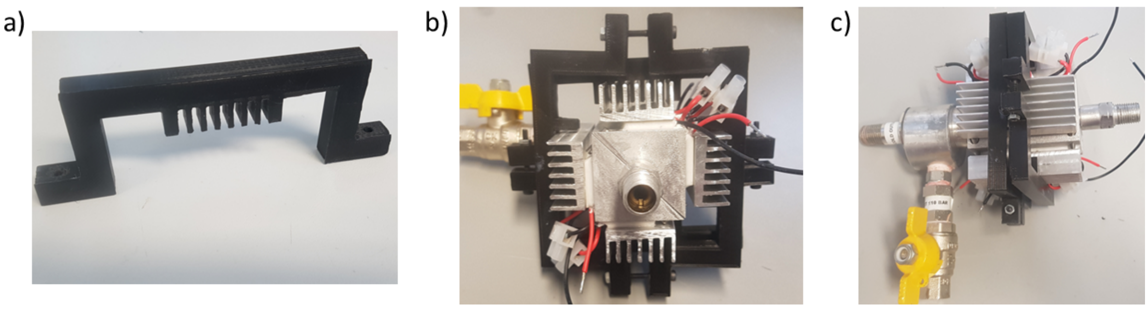

Figure 2.6: Photographs of (a) the PLA clamps designed to secure the heatsinks on the prototypes and (b) front and (c) side views of assembled prototype on the vortex tube.

The electric potential and current of the EHUs were measured as a function of the TEG's temperature gradient, which is altered by varying the pressure of the inlet gas in the vortex tube. Additionally, the performance of the devices was studied under various load resistances and their maximum output power was determined.

For all measurements the commercial TEGs were connected in series, in order to achieve the highest voltage. The data was acquired continuously using a microprocessor connected to *LabView* to measure electric voltage and current, and a *PicoLog* from *Pico Technology* to measure the temperature.

2.4 Experimental Results

Since the surface of the hot tube takes a couple of minutes to warm up after the gas flow starts, as seen in Section 2.1, it is important to determine how long it takes for the TEG's temperature gradient to stabilize. For that purpose, the temperature gradient was measured continuously for the three prototypes with heatsinks under the same conditions.

Figure 2.7 shows that, as the surface of the tube warms up, the hot surface of the TEGs also heats up, which leads to an increase of the TEG's temperature gradient until it reaches a maximum. As the the hot tube's surface stabilizes and the heatsinks heat up, the thermal gradient starts decreasing, until eventually it stabilizes. For the PLA geometry, the temperature gradient stabilizes around 21.3 °C after about 8 minutes. For the Al geometry, the temperature gradient stabilizes around 11.4 °C with the 10×10 mm^2 TEGs and around 4.1 °C with the 20×20 mm^2 TEGs, and in both cases it takes about 11 minutes for the temperature to stabilize. The PLA geometry not only stabilizes faster but also reaches the highest thermal gradient. However, since the number of TEGs and their dimensions vary between prototypes, it is not possible to predict which prototype is better without measuring their outputs.

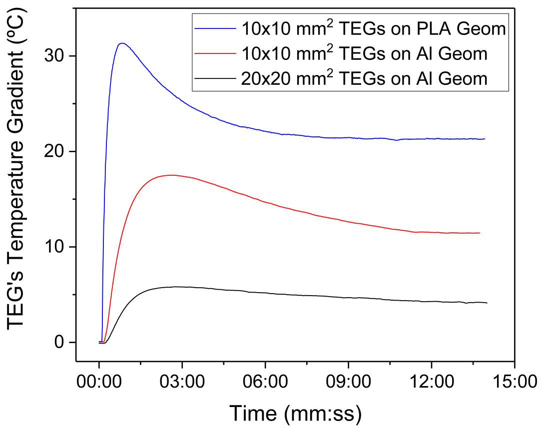

FIGURE 2.7: TEG's temperature gradient time dependency for the three prototypes with heatsinks, for an inlet gas pressure of 4 bar.

Hence, the output voltage was measured continuously in open circuit. The results presented in Figure 2.8(a) show that, for each prototype, the voltage curve has the same tendency as the TEG's temperature curve from Figure 2.7, as would be expected. In these conditions, the PLA geometry stabilizes at 1.01 V and the Al geometries stabilize at 0.76 V and 0.59 V with the 10×10 mm^2 TEGs and the 20×20 mm^2 TEGs, respectively.

The electric current was also measured continuously in open circuit and from Figure 2.8(b) we see that, similarly to what happens with the voltage, the current curves follow the same tendency as the TEG's temperature gradient. For the PLA geometry, the current stabilizes around 149.6 mA and the Al geometries made with $10\times10\,\text{mm}^2$ TEGs and $20\times20\,\text{mm}^2$ TEGs stabilize at 84.8 mA and 70.4 mA, respectively.

These results seem to indicate that the PLA geometry with $10\times10\,\text{mm}^2$ TEGs performs the best, while the Al geometry with $20\times20\,\text{mm}^2$ TEGs performs the worst.

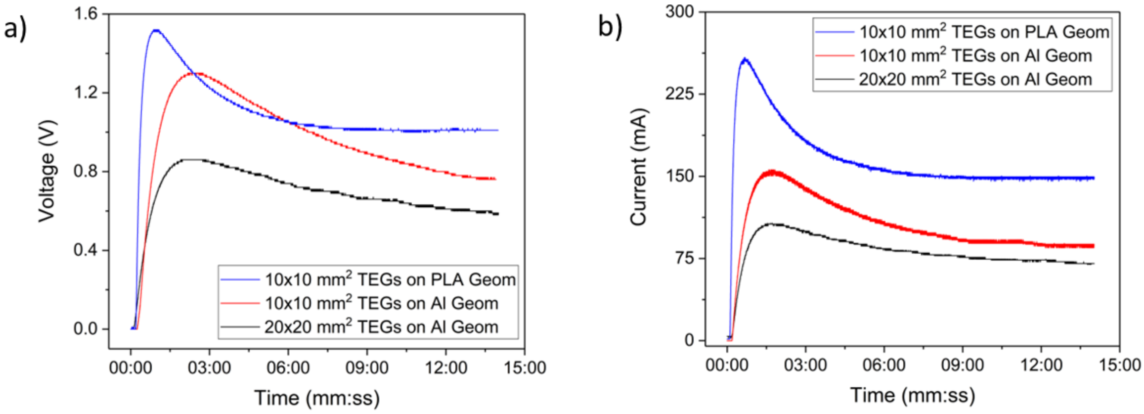

FIGURE 2.8: Output (a) voltage and (b) current time dependency measured in open circuit, for an inlet gas pressure of 4 bar.

These measurements were repeated for different temperature gradients by varying the vortex tube's inlet gas pressure, and the results are presented in Figure 2.9. Note that the temperature range is not the same for the three prototypes because, for the same measurement conditions, the TEG's temperature gradient is different for each prototype.

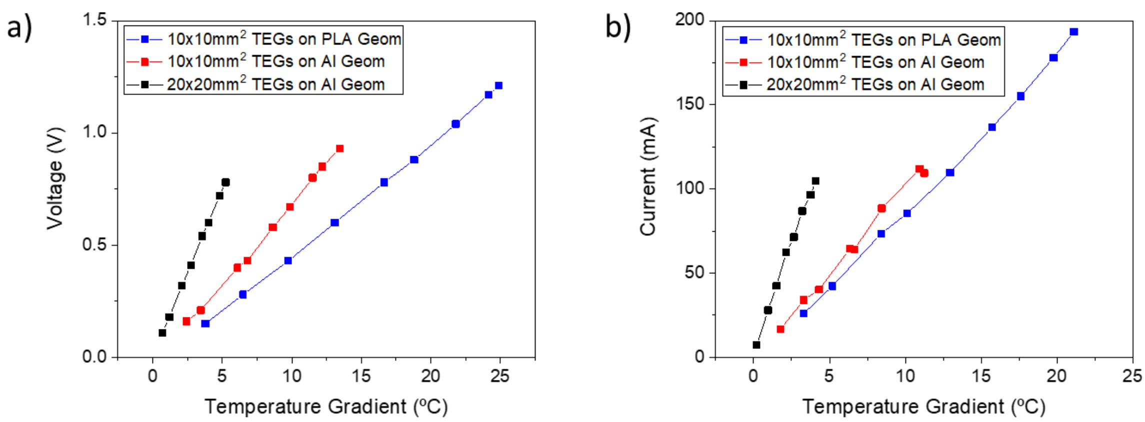

FIGURE 2.9: Output (a) voltage and (b) current measured in open circuit as a function of the TEG's temperature gradient.

The experimental results demonstrate that, for the same TEG temperature gradient, the prototype made of the Al geometry with the $20\times20\,\text{mm}^2$ TEGs performs significantly better than the other two prototypes, as would be expected since the 20×20 mm^2 TEGs ought to perform better than the 10×10 mm^2 TEGs.

To compare the performance of each TEG, the previous results were divided by the number of TEGs in each prototype (Figure 2.10). As anticipated, the output results for each TEG in the PLA and Al geometries with 10×10 mm^2 TEGs are similar. On the other hand, for the same thermal gradient, the output of each 20×20 mm^2 TEG on the Al geometry is more than five times superior than the other two prototypes. Therefore, we conclude that the 20×20 mm^2 TEGs perform more than five times better than the 10×10 mm^2 TEGs.

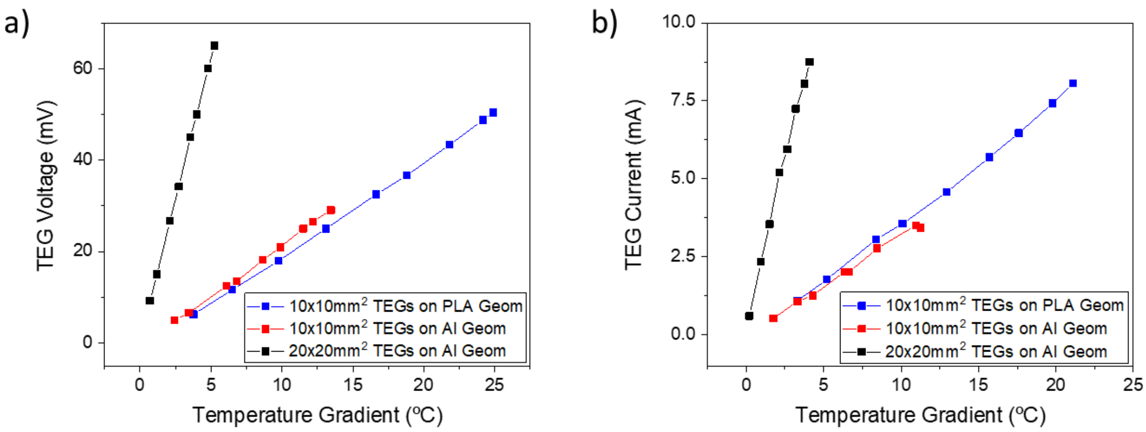

FIGURE 2.10: Normalized output (a) voltage and (b) current measured in open circuit as a function of the TEG's temperature gradient.

Despite the Al geometry with 20×20 mm^2 TEGs performing the best for the same thermal gradient, it is important to keep in mind that, for the same measurement conditions, the thermal gradient and therefore the output of each prototype isn't the same (as seen in Figure 2.8). Considering the applications of the prototypes, we are more interested in comparing the performance of the three prototypes under the same measurement conditions, in which case the best results are obtained with the prototype made of 10×10 mm^2 TEGs on the PLA geometry.

Lastly, to determine the maximum power and internal resistance of each prototype, their output was measured with different load resistances, for different temperature gradients. In Figure 2.11, the experimental results of the output voltage and current of the PLA geometry with 10×10 mm^2 TEGs, as well as its output power calculated as $P = VI$, are shown as a function of the load resistance. As expected, as the load resistance increases, the electric voltage increases and the current decreases. The maximum power is achieved when the load resistance equals the internal resistance of the device. At $\Delta T = 13.0\,°C$, the maximum power is 22.1 mW and its internal resistance 5.76 Ω.

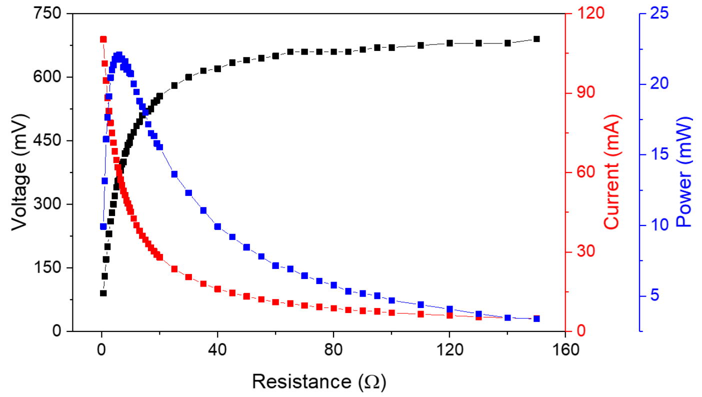

FIGURE 2.11: Output voltage, current and power as a function of the load resistance for the PLA geometry prototype at a TEG's temperature gradient of 13.0 °C.

These measurements were repeated at different temperature gradients and the results can be found in Appendix A, where the same tendencies were observed. The typical voltage-current curves and the power output as a function of the output voltage are shown in Figure 2.12. The maximum output power of this prototype ranges from 7.0 mW at 6.9 °C to 37.0 mW at 16.9 °C.

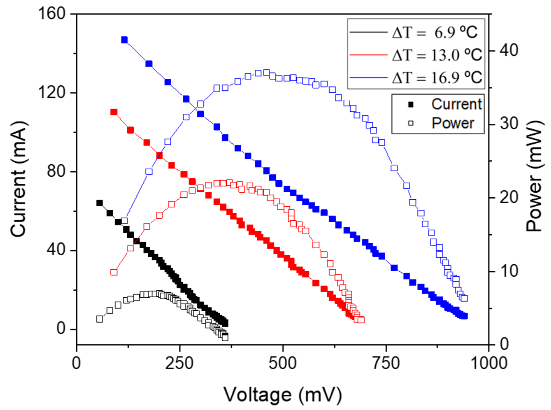

FIGURE 2.12: Current-voltage curves (solid squares) and power output (open squares) at different TEG temperature gradients for the PLA geometry prototype.

These measurements were repeated for the other two prototypes and the results can also be found in Appendix A where similar behaviors were observed. The results for the maximum power as a function of the TEG's temperature gradient are presented in Figure 2.13(a) and the device's internal resistance as a function of the TEG's effective temperature (estimated as the average between the temperatures of the hot and cold sides of the TEGs) are shown in Figure 2.13(b). Once again, the temperature range is not the same for the three prototypes because, for the same measurement conditions, the TEG's temperature gradient and effective temperature are different for each prototype.

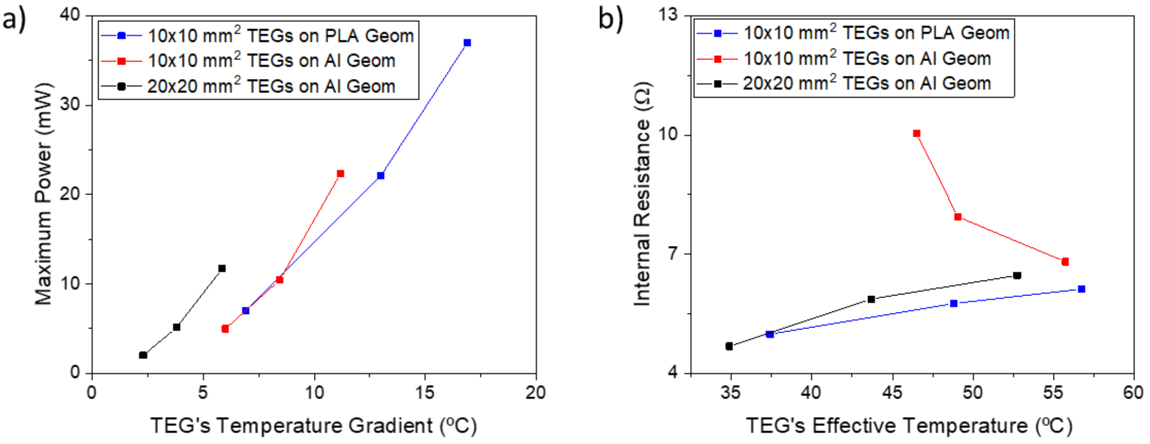

FIGURE 2.13: (a) Maximum power output as a function of the TEG's temperature gradient. (b) Internal resistance as a function of the TEG's effective temperature.

As would be expected, the output power increases with the thermal gradient. For the same temperature gradient, the Al geometry with $20\times20\,mm^2$ TEGs has the highest power, however, as explained before, because the thermal gradient isn't the same for the prototypes under the same measurement conditions, this does not imply that this prototype is the best.

As for the measured internal resistance, it is expected that it increases with temperature, however, for the $10\times10\,mm^2$ TEGs on the Al geometry, its internal resistance slightly decreases as the effective temperature increases. This results may be due to the incorrect positioning of the thermocouples during the measurements and therefore, the predicted effective temperature of the TEGs may be wrong.

Table 2.1 summarizes the outputs of each prototype when their power is at its maximum, for an inlet gas pressure of approximately 5 bar, and it shows that, under these conditions, the $10\times10\,mm^2$ TEGs on the PLA geometry generate the highest power.

TABLE 2.1: Maximum output generated by each prototype for a inlet gas pressure of 5 bar

Prototype	ΔT (°C)	V (mV)	I (mA)	P (mW)
$10\times10\,mm^2$ TEGs on PLA Geom	16.9	460	80.5	37.0
$10\times10\,mm^2$ TEGs on Al Geom	11.2	360	62.2	22.4
$20\times20\,mm^2$ TEGs on Al Geom	5.0	260	45.0	11.7

From these experimental results, it is concluded that, even though the prototype with $20\times20\,mm^2$ TEGs on Al geometry shows the best performance for a fixed thermal gradient, the prototype with $10\times10\,mm^2$ TEGs on PLA geometry has a much higher thermal gradient than the other two prototypes when the measurement conditions are fixed and therefore has the best performance.

It should be noted that these results were obtained for an inlet gas pressure between 2 and 5 bar, but in a gas distribution system the inlet pressure would be higher, and consequently so would be the surface temperature of the tube, which would lead to even higher outputs.

Chapter 3

Innovative Flexible Radial TEGs

This chapter takes a different approach to the EHU and focuses on exploring a flexible, screen-printed radial TEGs that can be retrofitted around the vortex tube's hot end tube.

In the first section, *COMSOL* simulations were performed to study the effect of the thermoelectric stripes dimensions on their temperature gradient and on the TEGs power output.

Then, a general overview of the methods adopted in this work to produce the thermoelectric thin films and TEGs is presented, followed by the characterization of the thin films, which is broken down into physicochemical and morphological analysis, transport properties and mechanical stability.

Lastly, the produced TEGs were tested on the vortex tube and their internal resistance and output power were measured. As a proof of concept, a prototype with 20 TEGs connected in series was printed and tested.

3.1 Numerical Simulations

Because the thermal gradient is created between the surface of the hot tube and the environment, the flexible TEGs are designed in a radial shape to go around the tube and are composed of ten thermoelectric stripes connected by electric contacts, as shown in Figure 3.1.

The power generated by the device depends not only on the thermal gradient but also on its electrical conductivity, both of which are affected by the thermoelectric stripes dimensions. Therefore, *COMSOL* simulations were performed to optimize the length, width and thickness of the stripes.

FIGURE 3.1: Schematic illustration of the designed radial TEG composed of thermometric stripes (black) and electric contacts (grey).

The simulations were performed using *COMSOL* modules *Heat Transfer in Solids*, *Electric Currents* and *Electrical Circuit*, and *Thermoelectric Effect* from *Multiphysics*. The hot side of the stripes was set to a constant temperature of 60 °C and the materials used were Bi_2Te_3 for the thermoelectric stripes and silver for the electric contacts, both from the *COMSOL* library.

The length, width and thickness of the thermoelectric stripes were varied individually, and the results of the stripes' temperature gradient and the TEG's output power are presented in Figure 3.2.

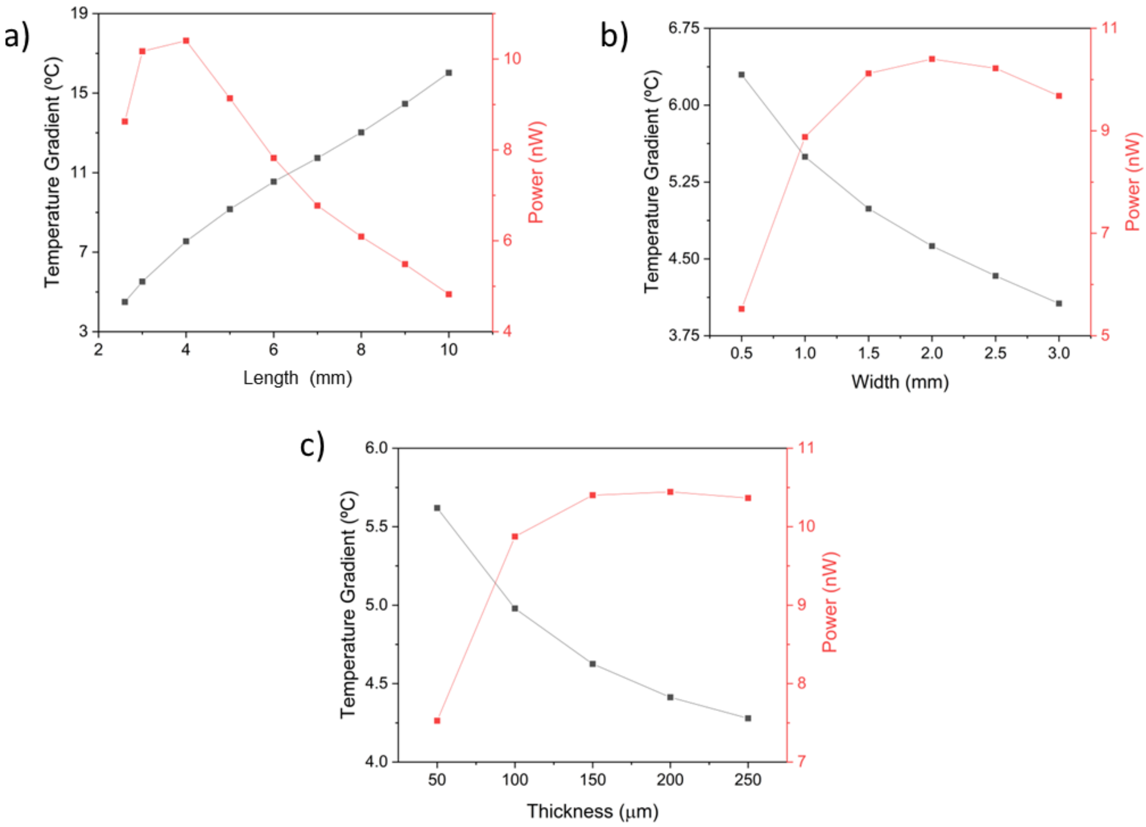

FIGURE 3.2: Simulation results for the influence of (a) the length, (b) width and (c) thickness of the thermoelectric stripe on its temperature gradient and on the device's output.

Regarding the stripe's length, it ranged from 2.5 to 10 mm while the width and thickness were fixed at 2 mm and 150 µm, respectively. Initially, as the length increases, so does the thermal gradient and, consequently, the output voltage. However, since the electric resistance of the stripe will also increase with the length, the output power increases until it reaches a maximum, after which the resistance becomes too high and the output power starts dropping, as we see in Figure 3.2(a). The maximum output power reached was 13.4 nW at a length of 4 mm.

When it comes to the stripe's width, it ranged from 0.5 to 3 mm while the length and thickness were constant at 4 mm and 150 µm, respectively. From Figure 3.2(b) it is seen that as the width increases, heat dissipates more easily, and therefore the thermal gradient decreases, but the resistance of each stripe also decreases. Thus, the output power increases with the width until it reaches a point after which the temperature gradient is too small and the power starts slowly decreasing. The maximum output power achieved was 10.4 nW for a width of 2 mm.

Finally, the stripe's thickness ranged from 50 to 250 µm, while the length and width were fixed at 4 mm and 2 mm, respectively. Figure 3.2(c) shows that, similarly to what happens with the width, as the thickness increases, heat dissipates better and the thermal gradient decreases. However, the resistance also decreases, and therefore the output power increases with the thickness until reaching a maximum, after which it starts slowly decreasing. This maximum was reached at 150 µm at a value of 10.4 nW.

Based on these results, the ideal dimensions for the stripes are $4 \times 2 \times 0.150\,mm^3$. The length and width of screen-printed stripes are easy to adjust by changing the printing design. However, their thickness depends on the viscosity of the ink and can only be increased by printing multiple layers, making it difficult to control. In this work, devices were printed with multiple thermoelectric layers to vary the thickness of the thermoelectric stripes and evaluate how much the output of the device actually depends on its thickness. Additionally, since the simulated output power was similar for lengths of 3 mm and 4 mm, the printed devices will have a stripe length of 3 mm.

3.2 Fabrication of the Printed Films and Devices

To characterize the thermoelectric ink produced and study the influence of its thickness and thermal treatment, films were printed with only the thermoelectric ink.

All films and TEGs were screen-printed on Kapton polyimide substrates, using the methodology described in this section.

3.2.1 Substrate Preparation

To improve the adhesion between the inks and the Kapton polyimide substrate, the substrates receive a chemical treatment that is based on the work of S.-J. Park *et al.* [38], and consists of immersing the substrates in potassium hydroxide (KOH) and hydrochloric acid (HCl) solutions.

Firstly, the substrates are immersed with a magnetic stirrer for 1 hour in a 10 wt% KOH aqueous solution that results from the combination of ultra-pure water with 85 % solid KOH. This first part of the treatment breaks the C-N bond on the substrate's surface and introduces a hidroxyl group that is soon replaced by potassium, improving the adhesion and roughness of the surface.

Next, the substrates are washed for 2 to 3 minutes in running water to remove the excess KOH and are then submerged in a 10 wt% HCl aqueous solution for 5 minutes with a magnetic stirrer. This solution neutralizes the surface by reintroducing hydrogen in place of potassium, increasing the chemical interactions between the substrate and the ink to be printed on top of it.

Finally, the substrates are once again washed with water and dried.

3.2.2 Preparation of the Thermoelectric Ink

The thermoelectric ink used in this work is made of n-type Bi_2Te_3 powder with a grain size of around 50 µm.

To make the ink, the powder must be mixed with an organic binder, like a polymer, which promotes flexibility and has low thermal conductivity. However, these materials also have low electrical conductivity and the contact resistance between organic and inorganic materials is high [39]. A. L. Pires *et al.* [40] found that doping polyvinyl alcohol (PVA) with orthophosphoric acid (H_3PO_4) increases its electrical conductivity.

For that, 6.89 g of PVA (Mw 89,000-98,000, 99 %) were added to 6.89 g of H_3PO_4 (85 %) dissolved in 60 ml of ultra-pure water, achieving a mass ratio of 1:1. After mixing, the solution is left for at least 6 hours in a silicon bath at 85 °C with continuous magnetic stirring. It is crucial that the bath's temperature never exceeds 90 °C as the polymer starts to degrade above that temperature.

For screen-printing, a small percentage of polymer will make the ink more viscous, leading to lower print quality. However, higher polymer concentrations lower the ink's electrical conductivity. Therefore, the ink used in this work was made of 35 wt% of PVA/H_3PO_4 and 65 wt% of Bi_2Te_3.

3.2.3 Screen-Printing

Screen-printing is a contact printing technique that uses a screen made of a fine mesh of silk or synthetic fibers to transfer a design to any planar substrate [41].

The design is printed on the mesh by applying a photosensitive emulsion to the mesh, placing the photolith (a transparent sheet with the design) on top of the emulsion and exposing it to UV light to cure it. In this way, the emulsion underneath the designs will not be cured and can be removed with water, allowing ink to pass only through the intended design [41]. Figure 3.3(a) shows the screen-printing machine available at the Institute of Physics for Advanced Materials, Nanotechnology and Photonics (IFIMUP) facilities with a screen with multiple designs in place.

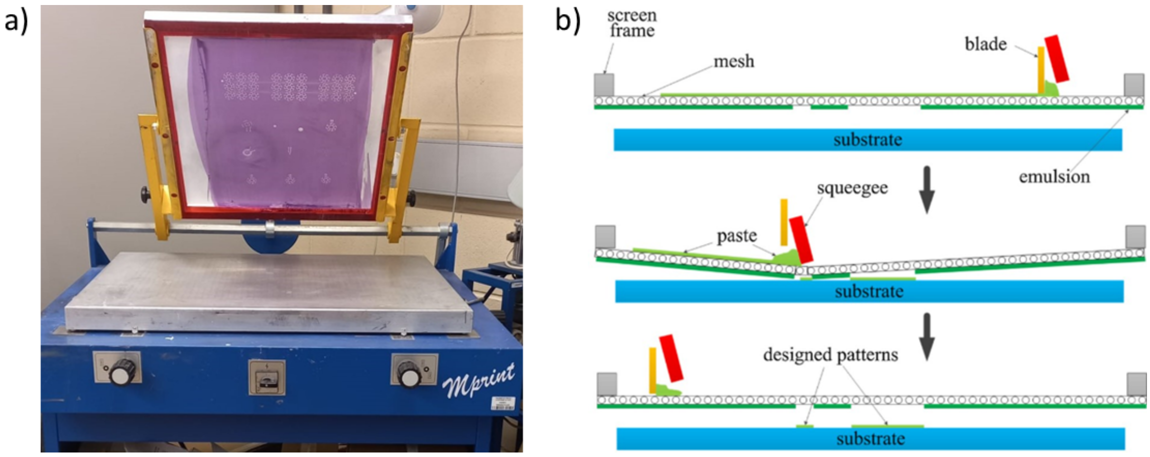

FIGURE 3.3: (a) Manual screen-printing machine at IFIMUP facilities. (b) Schematic presentation of the screen-printing technique [42].

The size of the openings of the mesh should be bigger than the material grains present on the ink, but it must be taken into account that the bigger the mesh, the lower the print definition.

To print, first the substrate is placed under the screen, aligned with the design. Then, ink is spread on the screen, on top of the design to be printed, without applying pressure to ensure a homogeneous print. Next, the ink is transferred to the substrate by passing the squeegee at a 45 ° angle in a continuous movement while applying pressure, as represented in Figure 3.3(b). In this work, the squeegee was always passed twice while applying pressure, once from top to bottom and once from bottom to top, to ensure a good transfer.

Since the thermoelectric ink tends to dry quickly, the mesh was cleaned with water and paper between prints to prevent clogging.

3.2.4 Printed Films

To study the influence of the thickness of the stripes and thermal treatment on its properties, $20\times10\,mm^2$ films were printed.

The thermoelectric ink was produced as described in Section 3.2.2 and screen-printed on chemically treated Kapton using the mesh PET 1500 27/120W, with a mesh-opening of 249 µm. By repeating the screen-printing process, films were printed with 1 to 4 layers in order to vary their thickness. To dry the ink, different curing temperatures were tested, as shown in Figure 3.4. For the first set of samples, here called "Set 1", each layer dried at room temperature before the next layer was printed and, after all layers had been printed, the films were heated at 80 °C for 10 minutes, followed by 193 °C for 3 minutes. For the second set, "Set 2", each layer was dried at 80 °C for 10 minutes and, after all layers had been printed, the films were heated to 193 °C for 3 minutes.

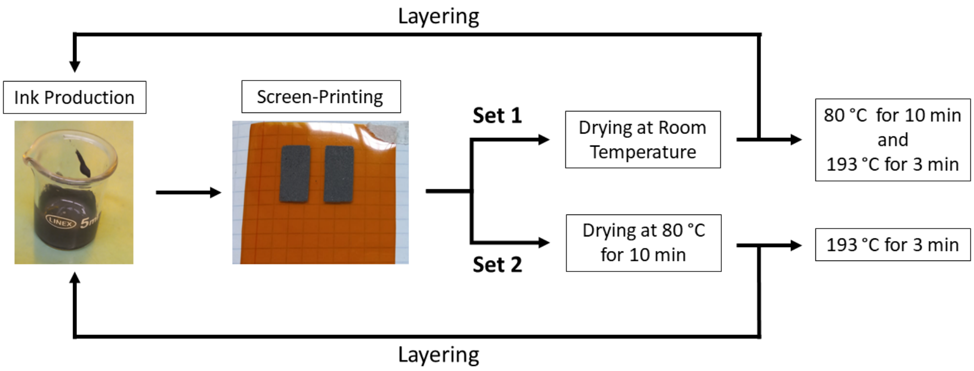

FIGURE 3.4: Film's production process.

From here on, the samples will be called *XL-SY*, where *X* is the number of printed layers and *Y* the set (except for the sample with only 1 layer, for which the thermal treatment is equal for both sets and therefore is simply called 1L).

3.2.5 Printed TEGs

The printed radial TEGs are made of electric contacts and thermoelectric stripes, as explained in Section 3.1.

To produce the devices, the electric contacts are screen-printed first, followed by the thermoelectric stripes, as seen in Figure 3.5. In this way, the thermoelectric stripes do not undergo the thermal treatment required to dry the electric contacts.

First, the electric contacts are screen-printed on the chemically treated kapton substrate using a commercial silver conductive ink from *VFP*. The screen-printing process is the same as previously described and the mesh used was the PET 1500 90/48W with a mesh-opening of 55 µm, since the silver ink has low viscosity and a smaller mesh has higher resolution. After printing, the ink is dried at 150 °C for 10 minutes.

Afterwards, to ensure that the interface between the silver contacts and the thermoelectric stripes is stable over time, an intermediate layer of carbon conductive ink from *ELANTAS* is screen-printed on top of the silver contacts. For that, the device was aligned with the contacts pattern on the same mesh used to print the silver contacts, and the screen-printing process was repeated. Next, the device is heated at 120 °C for 10 minutes, to dry the carbon ink.

Lastly, the device was aligned with the thermoelectric stripes pattern on the mesh PET 1500 27/120W, and the stripes were screen-printed. Similar to the previous section, the thermoelectric stripes were printed with 1 to 4 layers and two sets of thermal treatments were carried out.

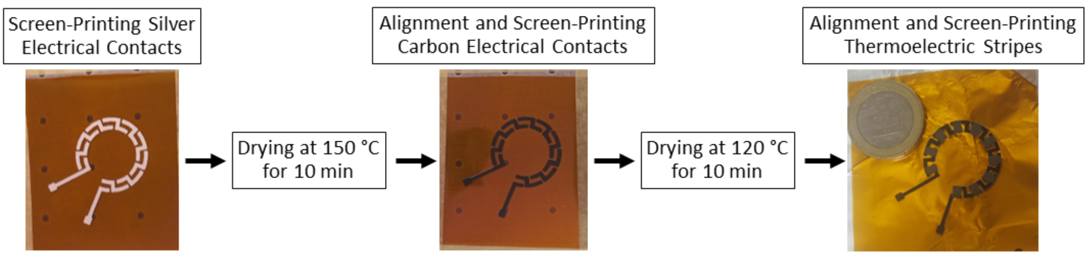

FIGURE 3.5: TEG's production process.

For these devices to be retrofitted around the vortex tube their center was cut using the circular blade shown in Figure 3.6 that was specifically made for this purpose.

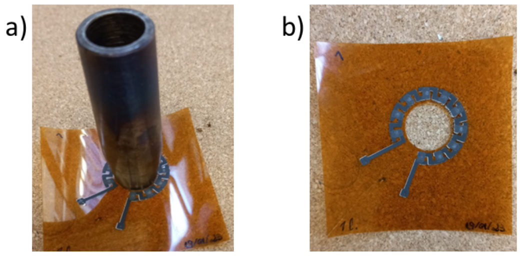

FIGURE 3.6: Cutting of the center of the TEG.

3.3 Characterization of the Films

To determine the effect of the number of layers and heat treatment on the films properties, they were characterized, starting with a physicochemical and morphological characterization, moving on to transport properties and ending with their mechanical stability.

3.3.1 Physicochemical Characterization

A thermogravimetric (TGA) and differential thermogravimetric (DTG) analysis were performed at the Institute of Nanoscience and Materials of Aragon (INMA) facilities using the *ImagenSATTGA Q5000* equipment from *TA instruments*. The analysis was performed between the ambient temperature and 1000 °C, with a step of 10 °C/min. Because of technical issues with the equipment, it wasn't possible to make this analysis for samples 4L-S1 and 4L-S2, but similar results to the ones seen in Figure 3.7 are expected for all films.

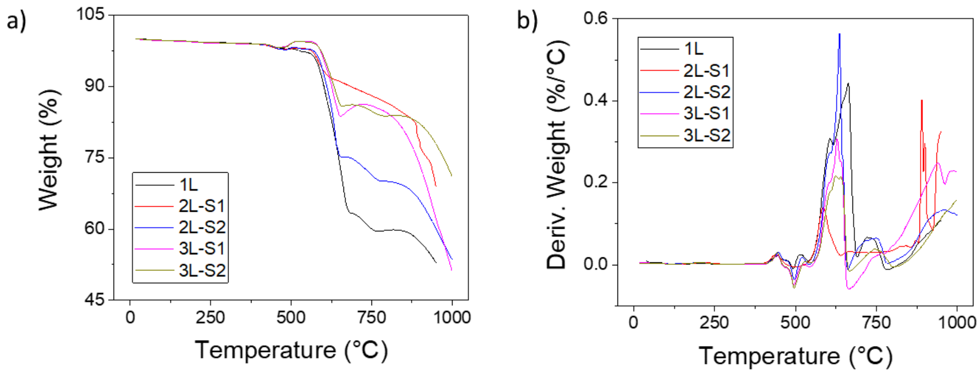

FIGURE 3.7: (a) TGA and (b) DTG analysis of the films.

Figure 3.7 shows that only above 500 °C significant variations on the weight occur, which is related with the thermal diffusion of the Bi and Te with some evaporation of Te due to their lower vapour pressure [40]. Nevertheless, from a practical point of view, Figure 3.7 shows that below 500 °C there aren't significant weight losses, meaning that the films aren't degraded at those temperatures. Since the vortex tube is not capable of reaching such high temperatures, it is concluded that the ink's stability would not be compromised for the intended application.

3.3.2 Morphological Characterization

The first thing expected to vary with the number of screen-printed layers is the thickness of the film. Therefore, the film's average thickness was measured with a *Digimatic Indicator* from *Mitutoyo* present at IFIMUP facilities. Figure 3.8 confirms that the thickness of the film is directly proportional to the number of printed layers, with each layer adding about 50 µm to the film's thickness, and that it is unaffected by the thermal treatment.

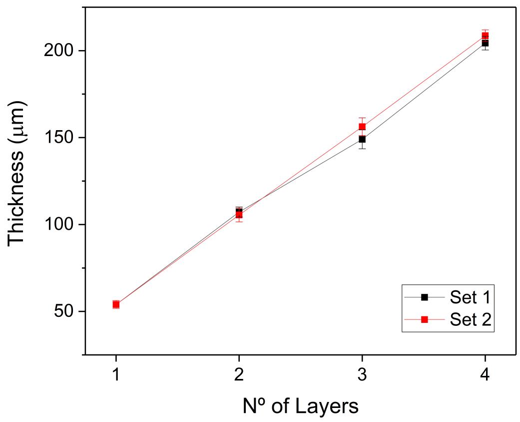

FIGURE 3.8: Thickness of the thermoelectric films.

To evaluate the film's surface uniformity, the *Sensofar PLµ 2300* confocal microscope available at INMA facilities was used to measure the surface roughness. Figure 3.9 shows the images of the film's surface taken with this device. Note that the vertical scale of the images does not refer to the thickness of the films but to the surface variation. The images show that, even though all films have generally uniform surfaces, their roughness increases with the number of layers. Additionally, some films have large pores at the surface, which are caused by the formation of air bubbles during the printing process.

To better understand how much the surface uniformity is affected by the number of layers and the heat treatment, the average variation of the surface's height (Δz) was measured and the results are presented in Figure 3.10. As expected, Δz increases with the number of layers but does not seem to be affected by the heat treatment, ranging from 20.6 to 68.4 µm for the first set and 20.6 to 71.8 µm for the second set. Even though these values seem significant when compared to the films' thickness, considering that the Bi_2Te_3 powder has a grain size around 50 µm, these Δz values are justifiable.

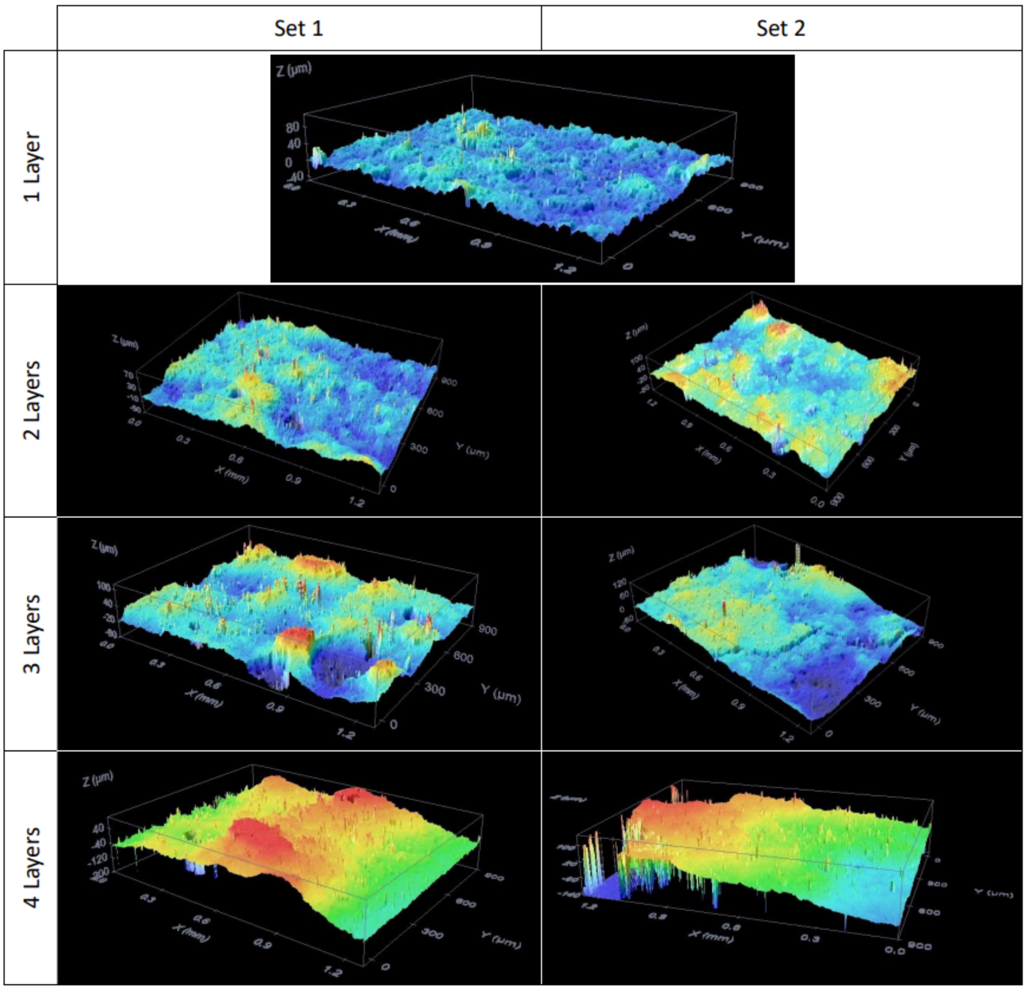

FIGURE 3.9: Films' surface images taken with a confocal microscope at INMA facilities.

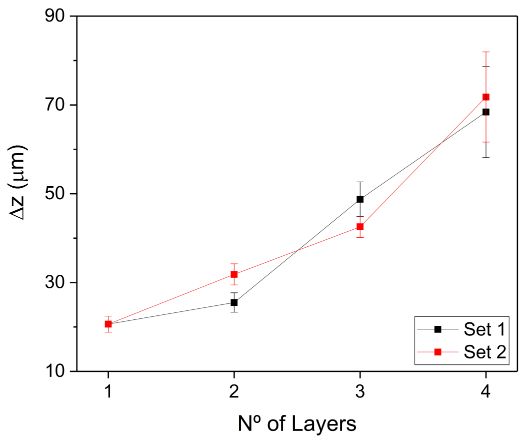

FIGURE 3.10: Surface height variation of each film.

Moving on to the scanning electron microscopy (SEM) analysis, the images from Figure 3.11 were taken using the field emission scanning electron microscope model *INSPECT-F50* available at INMA facilities. These images were collected in surface emission mode with a magnification of 1000 ×. On all films, it is observed that the Bi_2Te_3 particles are embedded in the polymer, which acts as a binder, indicating that the inorganic and organic materials mix well together, forming a homogeneous film. Moreover, the images confirm that the Bi_2Te_3 particles have an average grain size of 50 µm. On all images, small pores are visible on the surface of the films that are likely caused by the evaporation of the polymer. Regardless, the films are overall uniform, with low porosity and no visible cracks.

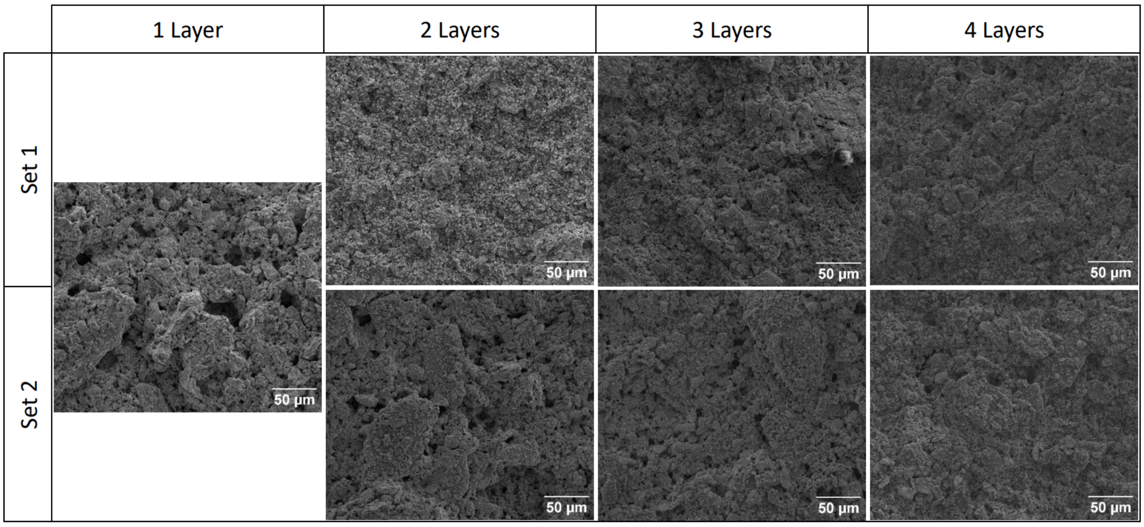

FIGURE 3.11: SEM images of the films' top surface, using 1000 × amplification.

Additionally, all films present the formation of microscopic crystals on their surfaces attached to the inorganic particles, as shown in Figure 3.12, which may be caused by H_3PO_4 crystallization [43].

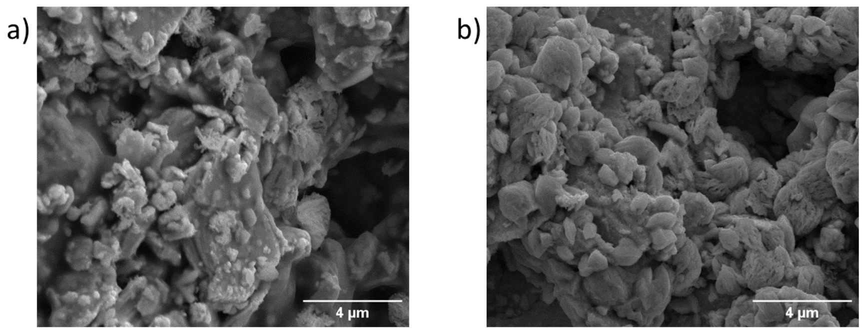

FIGURE 3.12: SEM images of the (a) 2L-S1 and (b) 2L-S2 films' surfaces using a magnification of 20000 ×.

Finally, to study the crystallinity of the films, the X-ray spectra were performed by the *Bruker SMART-APEX* diffractometer at INMA facilities, using Cu K_α radiation at a wavelength of 1.54059 Å and measuring 2θ between 10° and 90°. Figure 3.13 shows several peaks corresponding to Bi_2Te_3, which indicates that the films are polycrystalline. The main reflections are obtained for 2θ and respective Miller indices at 17.60° (0 0 6), 27.88° (0 1 5), 38.07° (1 0 10), 41.46° (1 1 0) and 44.80° (0 0 15), which point to a rhombohedral $R\bar{3}m$ space-group structure. Since the Bi_2Te_3 reflections predominate on the diffraction pattern and there aren't differences between the patterns of the different films, it is concluded that the polymer does not affect the crystallinity of the printed films, nor does the number of layers or thermal treatments.

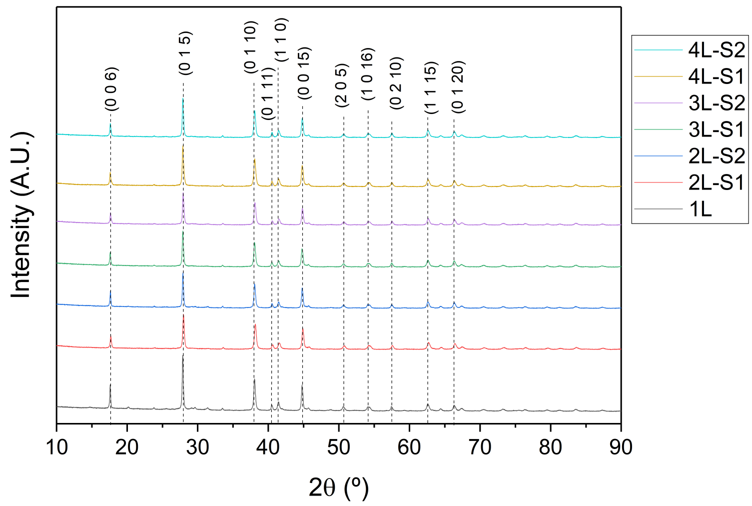

FIGURE 3.13: X-ray diffraction pattern of the thermoelectric films, with identification of the Miller indices of the main peaks belonging to the crystalline phase of Bi_2Te_3.

3.3.3 Transport Properties

To study the thermoelectric properties of each film, σ, S and PF were measured.

To serve as a point of reference, a pellet was made of the Bi_2Te_3 powder used to produce the thermoelectric ink and its transport properties were also measured. The results are presented in Table 3.1.

TABLE 3.1: Thermoelectric properties of the pellet made of Bi_2Te_3 powder

σ (S/m)	S (μV/K)	PF (μW/(K^{2}m))
2152.08	-100.54	21.75

Figure 3.14 presents the results obtained for each film, and it shows that the three thermoelectric properties measured are approximately constant for all the films, implying that the number of layers and the different thermal treatments do not alter the thermoelectric ink's properties.

Regarding the electrical conductivity, the films present values between 99 S/m and 101 S/m, which is much lower than the electrical conductivity of the thermoelectric powder and is caused by the addition of the polymer, that has low electrical conductivity.

The films' Seebeck coefficient is negative, as would be expected since an n-type thermometric powder was used, and it ranges from -99 to -95 µV/K. The obtained values are close to the Seebeck coefficient of the pellet because when two materials are mixed, S depends on the relationship between their electrical conductivities and the dominant value of S corresponds to that of the material with the best electrical conductivity [44], which in this case is the Bi_2Te_3 powder.

Since σ and S are constant for all films, so is the PF. It ranges from 0.88 to 0.98 µW/(K^{2}m), being lower than the Bi_2Te_3 pellet's since the electrical conductivity of the films is lower than the powder's.

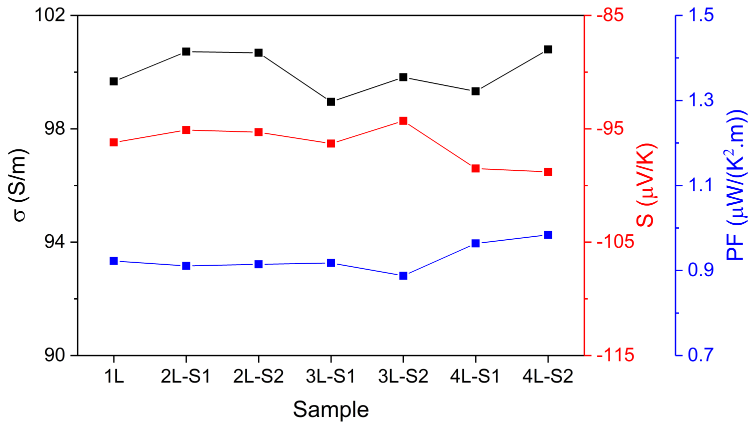

FIGURE 3.14: Electrical conductivity, Seebeck coefficient and power factor of the different films.

3.3.4 Preliminary Study of Mechanical Stability

Although the thermoelectric films are flexible, it is important to study how their properties change when mechanically deformed. For that purpose, the *AGS-X 10 kN* tensile tester from *Shimadzu*, available at University Rovira i Virgili (URV) facilities, was used to apply a vertical force and exert tension on the samples while their resistance was continually measured. Due to technical issues, it was only possible to perform this test for the films 1L, 3L-S1 and 4L-S2. The vertical displacement (Stroke) applied ranged from 0 to 0.5 mm for the samples 1L and 3L-S1, which corresponds to a radius of curvature of 7.10 mm, and from 0 to 0.2 mm for the 4L-S2 sample, for a radius of curvature of 7.22 mm. The Stroke was applied at a velocity of 50 µm/s and 25 cycles were measured for each film.

The results from the initial measurement cycles are presented in Figure 3.15.

For the film 1L, its resistance increases when tension is applied due to the separation of the inorganic particles of the ink, and decreases as it returns to its initial position because the particles re-establish contact. However, the film's resistance at its initial position increases with each cycle, which is probably due to the formation of microcracks.

For the other two films, as the deformation is applied, their resistance increases until a certain point, after which it decreases until the maximum deformation is reached. As the films return to their initial position, the resistance increases again before starting to decrease. This is due to the rigidity of these samples, which makes it harder for them to deform. Thus, as the Stroke is applied, the films initially deform and their resistance increases, but their rigidity prevents them from bending any further and the application of

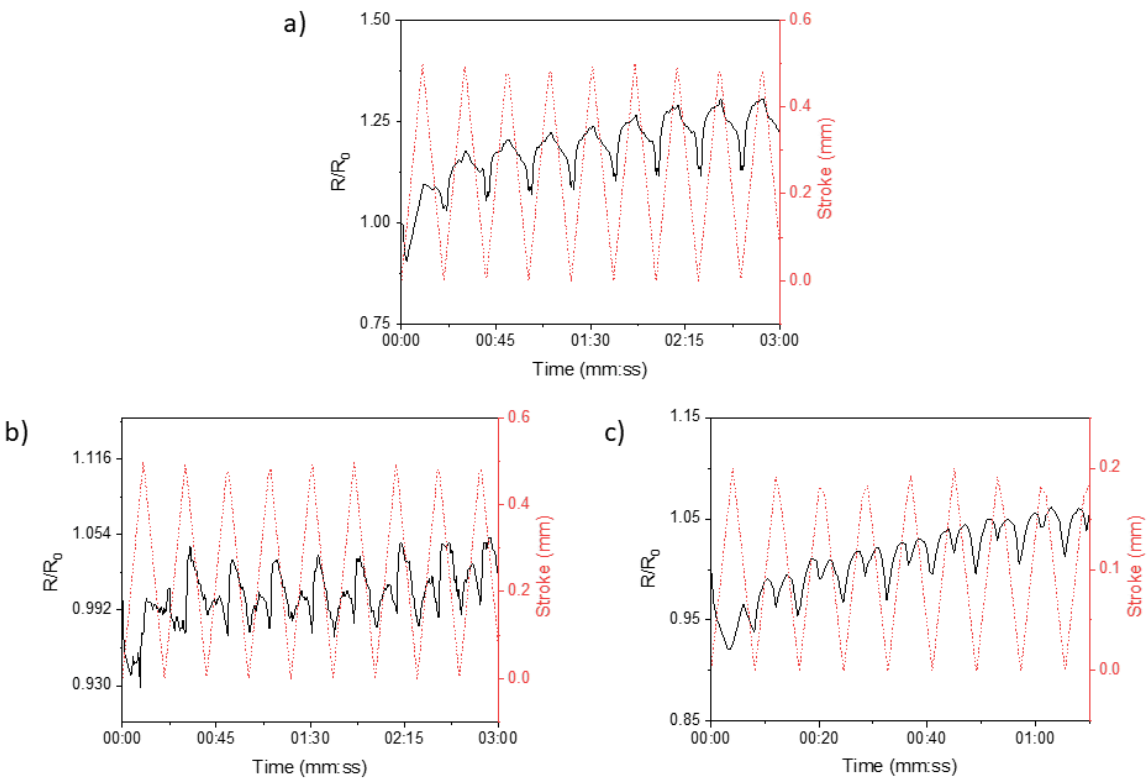

FIGURE 3.15: Relative resistance variation during the first deformation cycles of the films (a) 1L, (b) 3L-S1 and (c) 4L-S2.

the Stroke compresses the samples, causing their resistance to decrease. If a higher Stroke were applied, the films would probably crack and no longer be electrically conductive.

Figure 3.16 shows the evolution of the films' resistance at their initial position (Stroke = 0 mm) with each cycle. For the three films, the resistance increases with each cycle, but the curves seem to be stabilizing, which suggests that the films acquire some flexibility. The resistance of the sample 1L varies more than the sample 3L-S1, even though the applied Stroke was the same for the two samples, because the rigidity of sample 3L-S1 prevents the formation of micro-cracks and therefore its resistance varies less. The variation of the resistance of the samples 3L-S1 and 4L-S2 is very similar despite the applied deformation being lower for the latter, which further implies the loss of flexibility with increasing layers.

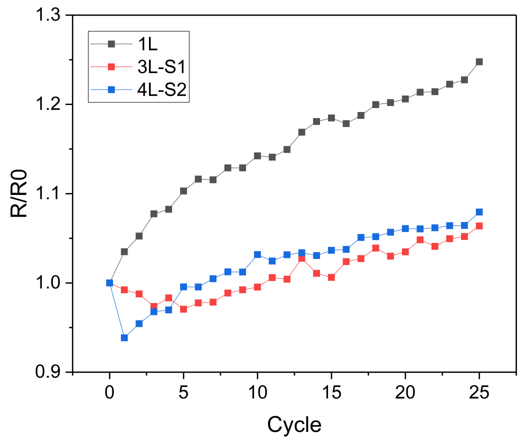

FIGURE 3.16: Evolution of the film's minimum resistance variation.

Although no conclusions can be drawn about the effect of the thermal treatments on the sample's flexibility, these results show that the increase in the films' thickness lowers their flexibility and that after 3 layers the films are too rigid and barely flexible.

3.4 Benchmark Tests

In addition to the characterization presented in the last section, radial TEGs were produced as described in Section 3.2.5 to evaluate their performance on the vortex tube.

First and foremost, it is important to measure the device's thickness because it is an indicator of the maximum number of TEGs that could be stacked on the vortex tube. A *Digimatic Indicator* from *Mitutoyo* was used to measure the thickness of the device where the thermometric ink is in contact with the electric contacts and, in that way, the thickness of the Kapton substrate, electric contacts and thermoelectric ink were all measured collectively. Figure 3.17 shows that the device's thickness increases with the number of layers, as expected, and there isn't a significant difference between the two sets. Theoretically, the maximum number of devices that can be retrofitted on the vortex tube is 560 for the TEGs with 1 layer and around 250 for 4 layers, assuming that the device's thickness is the limiting factor.

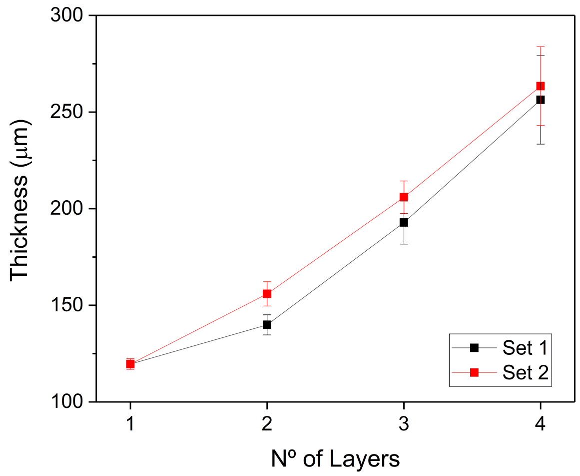

FIGURE 3.17: TEG's maximum thickness.

To evaluate the TEGs performance, they were retrofitted on the surface of the hot end tube of the vortex tube, as shown in Figure 3.18(a). The surface temperature of the hot tube was approximately 60 °C throughout all measurements. The TEG's electric voltage was measured in open circuit and, for all devices, voltages around 6 mV were measured for temperature gradients of approximately 6 °C. The TEG's output power was obtained from [45]:

$$P = \frac{V^2}{4R_{int}}, \tag{3.1}$$

where V is the open circuit voltage and R_{int} is the device's internal resistance, measured with a multimeter.

The results are graphically presented in Figure 3.18(b). As expected, the internal resistance decreases with the increase of the thermoelectric stripes' thickness and the devices belonging to the second set have a slightly higher resistance than those from the first set. Consequently, the devices from Set 1 have a higher output power than those from Set 2, and the best performance is achieved with the devices with four layers of thermoelectric ink. The maximum power measured was 134 nW for the TEG 4L-S1.

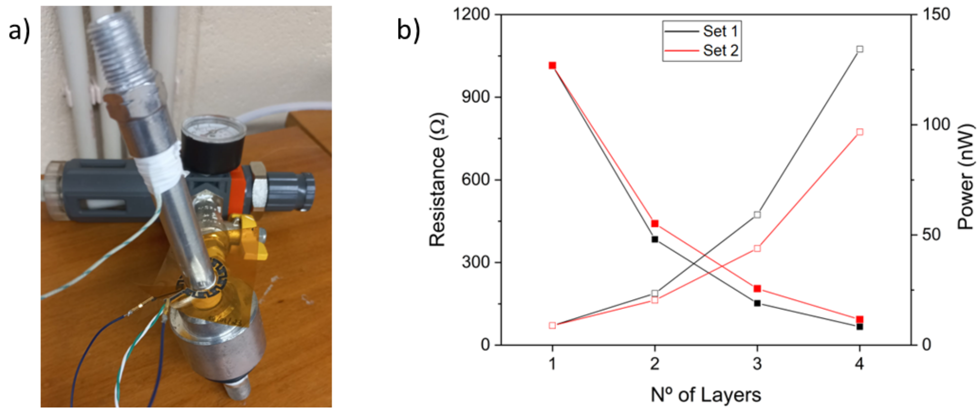

FIGURE 3.18: (a) Setup for measuring the electric voltage of radial TEGs retrofitted on the vortex tube. (b) Internal resistance (solid squares) and power outputs (open squares) of the different TEGs.

These results are not in agreement with the *COMSOL* simulations from Section 3.1, which predicted that the output power would first increase rapidly with the thermoelectric stripes' thickness and then slowly decrease. This happens because those simulations also predicted that the temperature gradient would decrease with the thickness but, in reality, it was observed that the number of layers did not significantly influence the temperature gradient. This is due to the simulations considering pure Bi_2Te_3 and pure silver for the thermoelectric stripes and electric contacts, respectively, and not considering the influence of the Kapton substrate.

These results indicate that the optimal device should have four screen-printed layers of thermoelectric ink. However, it is important to consider that the device's flexibility worsens with increasing layers, making it less durable and less desirable for the intended application.

3.5 Proof of Concept

To test the feasibility of stacking multiple TEGs on the hot surface of the vortex tube, a prototype was designed with 20 radial TEGs connected in series, as shown in Figure 3.19. Taking advantage of the flexibility of these devices, the prototype is designed in such a way that the electric connectors can be bent so that the TEGs can be stacked one in front of the other. The manufacturing procedure for this device was the same as described in Section 3.2.5, except that the thermoelectric powder used to formulate the ink was from a different brand and had a higher Seebeck coefficient. Only 1 layer of the thermoelectric ink was printed to ensure the device's mechanical stability, but more layers could be added to improve its output.

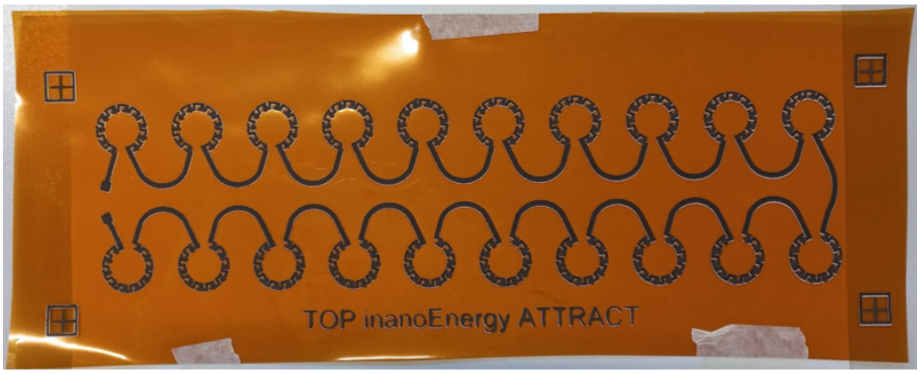

FIGURE 3.19: Screen-printed prototype consisting of 20 radial TEGs connected in series.

After printing and cutting the prototype, it was placed around the vortex tube as shown in Figure 3.20(a). Once again, the internal resistance and open circuit voltage were measured to determine the output power. Right after being produced, the device's internal resistance was 12.97 kΩ. However, the measurements were made over a month after its manufacture and its resistance increased to 104.5 kΩ, which is mostly due to the prototype being cut manually and continually bent during the process. For an average tube surface temperature of 60 °C, an open circuit voltage of 204.6 mV was measured, which translates to an output power of 100.15 nW.

If the device is arranged in a more compact configuration, as can be seen in Figure 3.20(b), what limits the maximum number of TEGs that can be placed on the tube is not their thickness but the space taken up by the connectors between TEGs. When arranged like this, the prototype occupies a minimum of 6 mm of the tube's length, meaning that 11 more prototypes like this one can fit on the tube, and an output power of 1.10 µW could

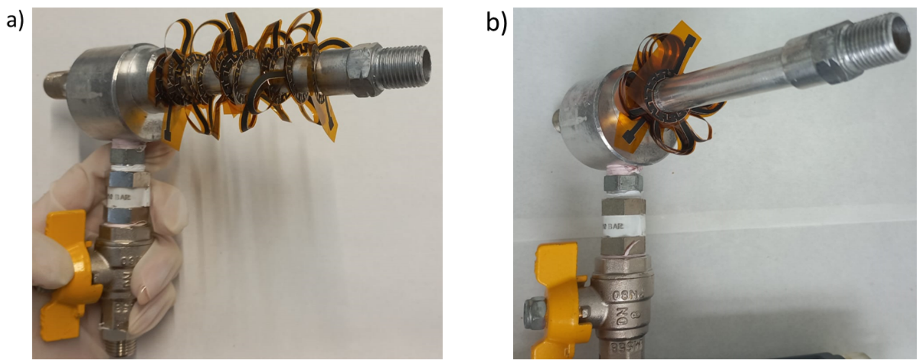

FIGURE 3.20: Prototype retrofitted on the vortex tube occupying (a) the entire length and (b) the minimum length of the tube.

be generated. Besides, if more layers of the thermoelectric ink were printed, this output could be further increased. According to the results from the previous section, the output would double just by adding one more layer to the stripes.

Chapter 4

Test of the Developed Prototypes

The goal of this work is to power a PU for in-situ monitoring, hence, the developed prototypes need to produce enough energy to feed sensors and send data wirelessly.

The screen-printed radial devices produced in Chapter 3 have the potential to generate output powers in the order of μW, which is not enough to feed a PU. The prototypes from Chapter 2 however, generate enough energy for this application. In particular, the prototypes made of $10\times10\,\text{mm}^2$ TEGs on Al and PLA geometries perform the best and therefore were used to power a PU developed by inanoEnergy [Figure 4.1(a)].

The PU is capable of boosting the voltage generated by the thermoelectric prototype to 5 V, feed a sensor with an average voltage of 3.5 V, read the sensor's signal and send the data through a wireless communication protocol.

Before testing with a gas sensor, the PU's input was connected to its output, as seen in Figure 4.1(b), allowing it to read the electric signal to be fed to the sensor and check that it is working properly. Additionally, the charge of the PU's capacitors and its output were also measured with a oscilloscope. These tests were made using the PLA prototype to power the PU, and the TEG's temperature gradient was varied by changing the inlet gas pressure, in order to check the PU's response to different outputs from the EHU.

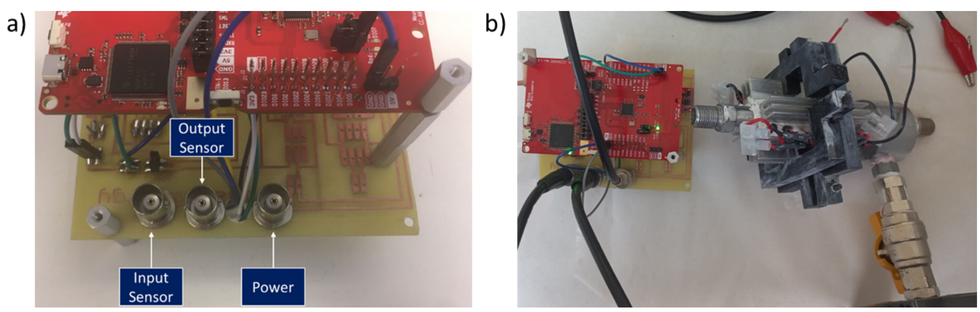

FIGURE 4.1: (a) PU developed by inanoEnergy. (b) Setup used to power the PU.

The graphs from Figure 4.2 show that the capacitors are charged to 5 V and, after reaching that value, the capacitors discharge, leading to a peak of 3.5 V at the PU's output, which is followed by the reading at the PU's input and the transmission of that data. For TEG's temperature gradients of 13 °C and 20 °C, the signals period is of 650 ms and 420 ms, respectively. This difference is due to the EHU's output power increasing with the gradient and, therefore, charging the capacitor faster. Note that the capacitors do not discharge immediately after saturating because the PU has a minimum timeout of 140 ms to ensure that the threshold has truly been reached and the signal is stable.

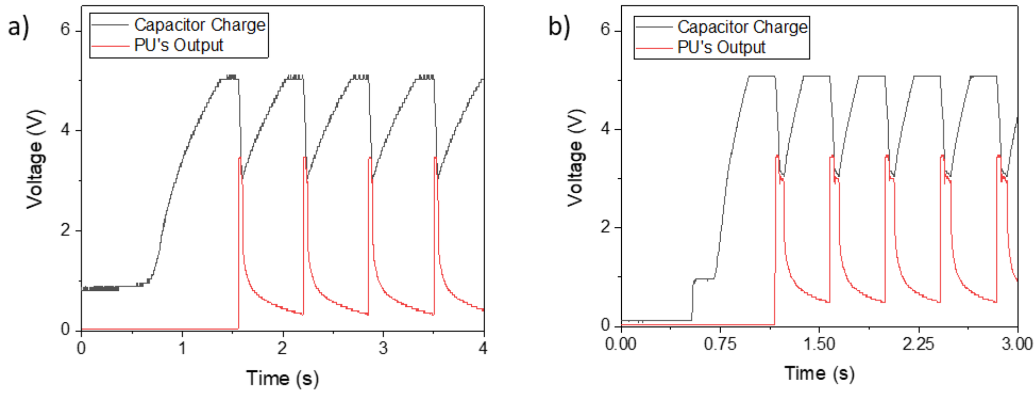

FIGURE 4.2: PU's capacitor charge and its output for a TEG temperature gradient of (a) 13 °C and (b) 25 °C.

Figure 4.3 shows the PU's output signal read by the PU's input and sent via the wireless protocol. Since the signal is only read when the output peak occurs, it is constant around 3.5 V and contains some noise that can be easily removed through signal processing. This confirms that the PU's output is constant over time, even if temperature fluctuations occur, and that it is capable of correctly measuring an electric voltage.

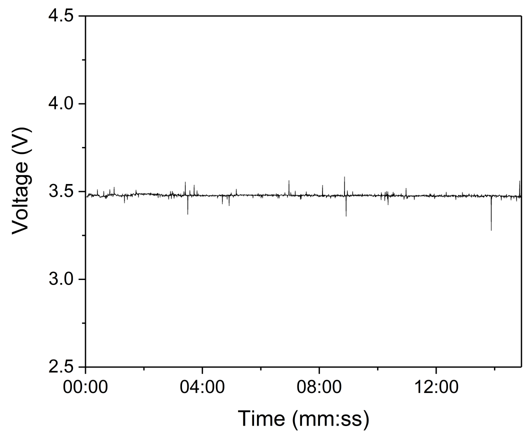

FIGURE 4.3: Electric voltage measured by the PU when its output and input are connected.

Finally, the PU was tested with a graphene sensor, whose resistance is sensitive to changes in the surrounding atmosphere. To measure the sensor's resistance (R_{sensor}), a voltage division circuit was used, as shown in Figure 4.4, so that the PU's output (V_{in}) is feeding the sensor connected in series with a resistance (R), and the PU's input reads the voltage drop caused by the sensor (V_{out}). The sensor's resistance can then be measured by:

$$R_{sensor} = \frac{R \times V_{out}}{V_{in} - V_{out}}. \tag{4.1}$$

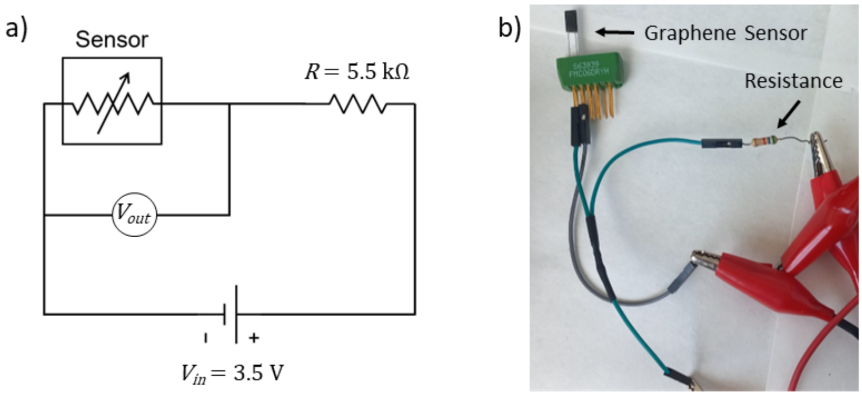

FIGURE 4.4: (a) Schematic representation and (b) actual setup of the electric circuit used to measure the sensor's voltage drop.

Before connecting it to the circuit, the sensor's resistance was measured at ambient conditions using a multimeter and a value of 6 kΩ was measured. This is consistent with the results shown in Figure 4.5(a), which were obtained using the PU supplied by the PLA prototype for a TEG temperature gradient of 20 °C. The figure shows that an average resistance of 6.21 kΩ is continuously measured and that at 4 minutes of measurement, by blowing on the sensor, the humidity in its surrounding atmosphere is increased, which causes its resistance, and consequently the measured voltage, to decrease.

The measurements were repeated using the Al prototype for a TEG temperature gradient of 18 °C, and the results are presented in Figure 4.5(b). An average voltage of 6.16 kΩ was measured at ambient conditions and once again, by blowing on the sensor at about 4 minutes into the measurement, a decrease in the sensor's voltage and resistance can be observed.

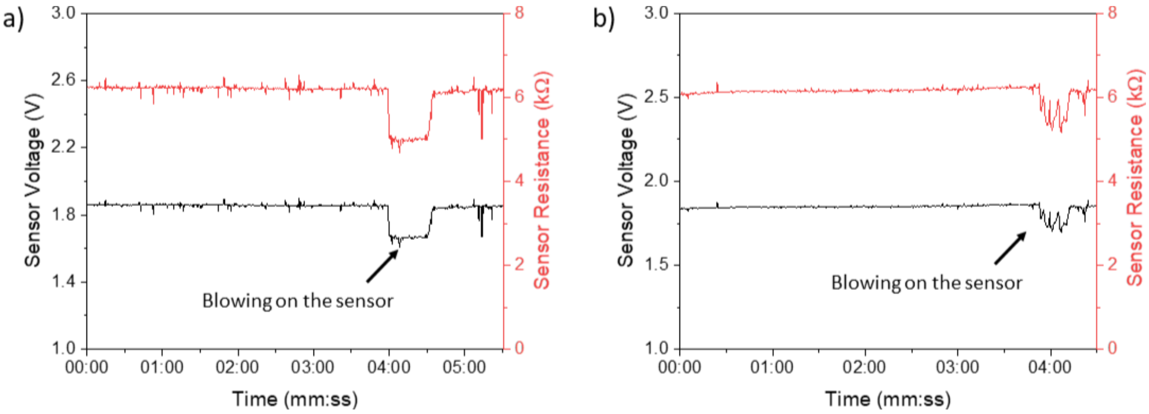

FIGURE 4.5: Sensor's output voltage and calculated resistance, measured with the PU connected to (a) the PLA and (b) the Al prototypes.

These results prove not only that the PU is capable of accurately reading sensor information and wirelessly sending it continuously, but also that the tested prototypes can produce enough energy to continuously power the PU. Therefore, either of the geometries can be used for the desired application, with the PLA geometry being the cheapest solution and the Al geometry the most robust.

Chapter 5

Conclusions and Future Work

5.1 General Conclusions

In this work, two approaches were employed towards the main goal of developing a thermoelectric EHU to be retrofitted on a vortex tube and power a PU for in-situ monitoring in a gas distribution network.

A study of the vortex tube's thermal outputs confirms that this device is capable of generating and maintaining high temperatures on its hot end tube's surface, sustaining an average surface temperature of 56.4 °C for an inlet gas pressure of 4 bar, making it a powerful tool for the desired application.

In the first approach, the EHU consists of commercial TEGs assembled on top of a geometry to be placed around the tube and uses Al heatsinks to enhance the thermal gradient. Based on *COMSOL* simulations, three prototypes were made. It was verified that the prototype made of $20\times20\,mm^2$ TEGs on the Al geometry has the highest power versus temperature gradient ratio. However, the temperature gradient created by each prototype is not the same under fixed measurement conditions. Table 5.1 presents the maximum outputs generated by each prototype under the same measurement conditions and shows that the prototype made of $10\times10\,mm^2$ TEGs on the PLA geometry produces the highest output power.

In the second approach, flexible radial TEGs made of ten thermoelectric stripes connected in series were screen-printed to go around the tube. Numerical simulations predicted that the ideal dimensions of the stripes were $4\times2\times0.150\,mm^3$, but since the stripes' thickness is difficult to control by screen-printing, multiple layers of the thermoelectric ink were printed and suffered different thermal treatments to study the effect on its thickness

TABLE 5.1: Maximum output generated by each prototype under the same measurement conditions

Prototype	ΔT (°C)	V (mV)	I (mA)	P (mW)
10×10 mm^2 TEGs on PLA Geom	16.9	460	80.5	37.0
10×10 mm^2 TEGs on Al Geom	11.2	360	62.2	22.4
20×20 mm^2 TEGs on Al Geom	5.0	260	45.0	11.7

and the material's properties. It was concluded that each layer increases the thickness by about 50 µm and that, even though the films are overall uniform and have low porosity, the surface roughness increases. The films' thermoelectric properties are approximately the same regardless of the number of layers or thermal treatment and their average values are presented in Table 5.2. The ink's S is almost the same as the thermoelectric powder used, however, σ and consequently PF are reduced by the addiction of the polymer, which has low σ. Additionally, TGA analysis shows that the films can endure temperatures up to 500 °C, ensuring that the devices wouldn't degrade when used for the intended application. A preliminary study of their mechanical stability indicates that their brittleness increases with their thickness and at 3 layers the films are too rigid and barely flexible.

TABLE 5.2: Average thermoelectric properties of the films

S (µV/K)	σ (S/m)	PF (µW/(K^{2}m))
-97	100	0.93

The developed TEG's output power was measured and it was verified that it improves with increasing number of printed layers due to its internal resistance decreasing. The highest output obtained was of 134 nW from the 4L-S1 device, for a tube surface temperature of 60 °C. Additionally, as proof of concept, 20 TEGs connected in series were screen-printed with one thermoelectric layer and, for the same tube surface temperature, an electric voltage of 204.6 mV, or 100.15 nW of power, was measured. Since the tube can fit 220 TEGs connected in series, potentially 1.10 µW could be generated, and this value could be increased if more thermoelectric layers were printed. Although this approach produces less energy than the first, these devices have the advantage of being lightweight, less bulky and easier to employ and, besides, are easy to manufacture and easily scalable.

Finally, because the first approach produced the best results, the prototypes made of 10×10 mm^2 TEGs on PLA and Al geometries were used to power a PU developed by inanoEnergy. It was verified that the power produced by the EHUs enables the PU to feed a graphene sensor with 3.5 V, correctly read the sensor's signal and send the collected data wirelessly at a minimum rate of $1.5\,s^{-1}$.

5.2 Technological Impact

The work done during this internship is integrated into the ATTRACT R&D&I PiPe4.0 and the MSCA-RISE SENSOFT projects. The aim was to develop a self-powered gas sensor IoT unit for in-situ monitoring and quality assessment. The project objectives were successfully achieved and the outcome is a cutting-edge device that has reached a Technology Readiness Level (TRL) of 5, namely by having been validated, demonstrating its functionality and performance.

The unit's self-powering capabilities eliminate the dependence on external power sources and batteries, and the device's minimal maintenance requirements ensure its long life span. Furthermore, the system can also adapt to a wide variety of gas mixtures with a wide range of compositions, and it has applications in a variety of industrial processes where continuous gas monitoring is necessary.

Commercializing this technology could provide numerous benefits, such as cost savings, improved data collection and analysis, and enhanced monitoring capabilities. Given its enormous potential for widespread implementation in real-world applications, inanoEnergy is currently assessing its commercial viability.

5.3 Future Work

As a complement to this work, additional steps could be taken to improve the developed EHUs of the two approaches.

Regarding the first approach, since the developed devices are already capable of powering a PU, a crucial step to evaluate their reliability and durability would be to test them under extreme tube surface temperatures and different atmospheric conditions to evaluate the effect on their output and its stability and verify their durability. Additionally, since in a real-life application the PU would need to feed and read multiple sensors, a more versatile PU should be developed and tested with these prototypes to check if they produce enough power to respond to the demands of a gas distribution network. Lastly, if all of these tests are successful, the devices could then be integrated into a gas distribution system and tested continuously for various months to evaluate their performance for the intended application.

As to the second approach, although the printed devices produce low outputs, their voltage could be increased by enhancing the thermal gradient. One strategy to accomplish that is to print radial metallic heatsinks on the opposite surface of the Kapton substrate to cool down the outer part of the thermoelectric stripes and improve their temperature gradient. Furthermore, a device should be printed with the maximum number of TEGs that can fit on the tube to confirm the predictions made from this work and test the device's feasibility and durability.

Appendix A

Outputs of Commercial TEG EHUs as a Function of Resistance

This Appendix contains the experimental results of the output voltage, current and power as a function of the load resistance, measured for the three prototypes made of commercial TEGs, at different temperature gradients, as well as the respective current-voltage and power-voltage curves.

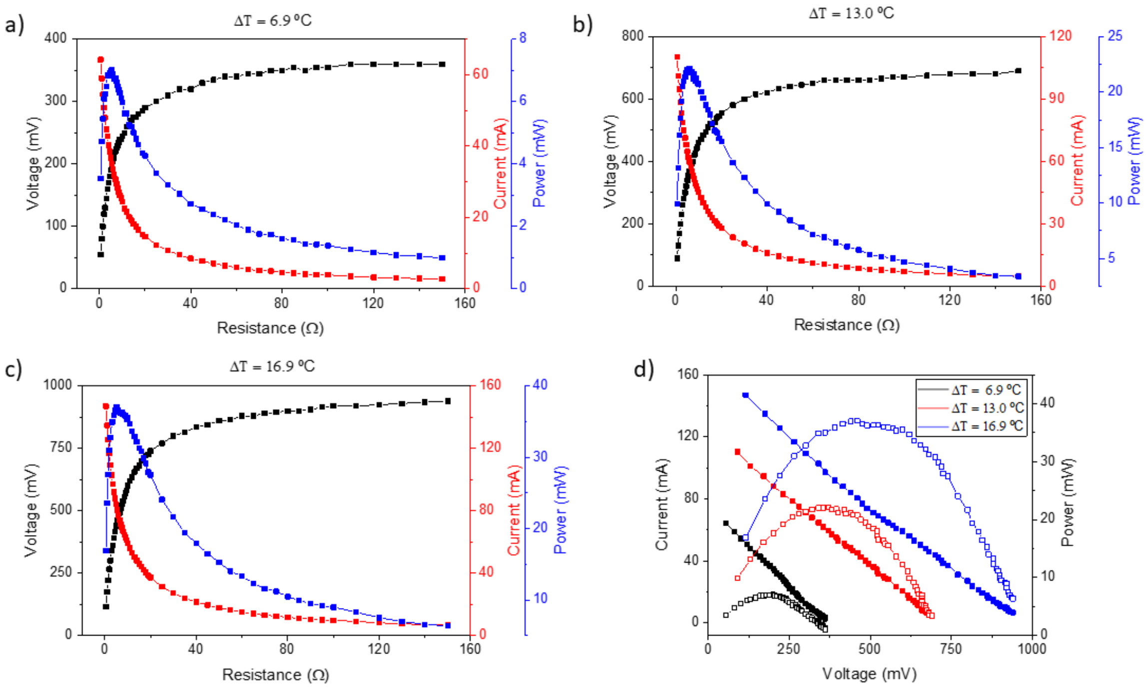

FIGURE A.1: Output voltage, current and power as a function of the load resistance at a TEG's temperature gradient of (a) 6.9 °C, (b) 13.0 °C and (c) 16.9 °C, and (d) output current (solid squares) and power (open squares) as a function of the voltage, of the PLA geometry with 10×10 mm^2 TEGs.

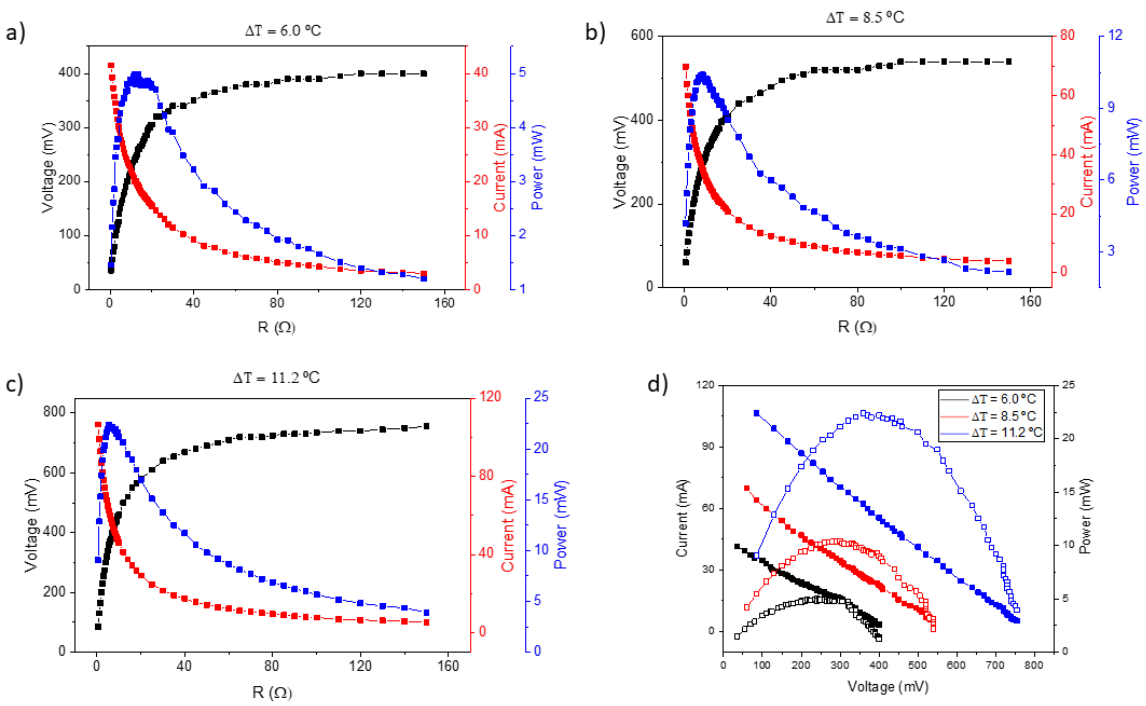

FIGURE A.2: Output voltage, current and power as a function of the load resistance at a TEG's temperature gradient of (a) 6.0 °C, (b) 8.5 °C and (c) 11.2 °C, and (d) output current (solid squares) and power (open squares) as a function of the voltage, of the Al geometry with 10×10 mm^2 TEGs.

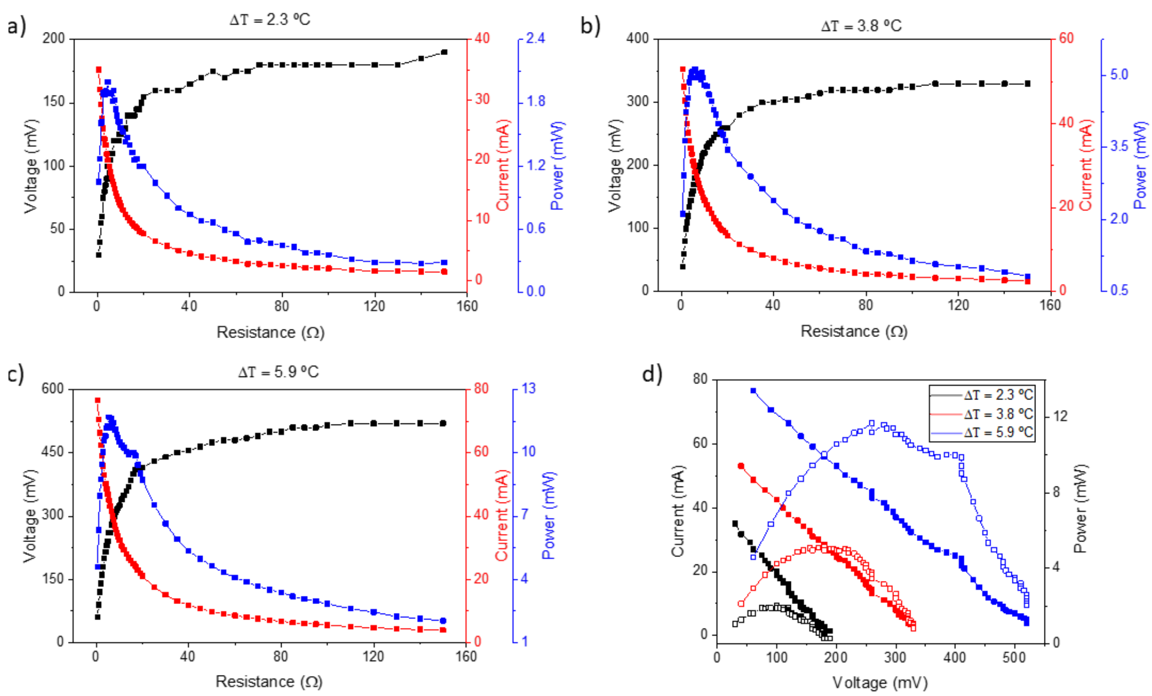

FIGURE A.3: Output voltage, current and power as a function of the load resistance at a TEG's temperature gradient of (a) 2.3 °C, (b) 3.8 °C and (c) 5.9 °C, and (d) output current (solid squares) and power (open squares) as a function of the voltage, of the Al geometry with 20×20 mm^2 TEGs.

Appendix B

FTIR Analysis of the Thermoelectric Films

Additional to the characterization presented on Chapter 3, the thermoelectric film's Fourier transform infrared (FTIR) spectra was measured using the *Bruker Vertex 70 FTIR* spectrometer available at INMA facilities. The spectrometer was used in transmission mode at wavelengths in the range of 4000 to 600 cm^{-1} and a resolution of 4 cm^{-1}. Since there isn't much information about the Bi_2Te_3 FTIR spectrum in literature, a film made only of the PVA/H_3PO_4 polymer was printed and cured at 80 °C for 10 minutes and 193 °C for 3 min, to compare its spectra with the films'. Figure B.1 shows that most of the absorption peaks present in the films' spectra correspond to absorption from the polymer, which is mainly caused by O-H, C-H and C=O stretching and water absorption [46].

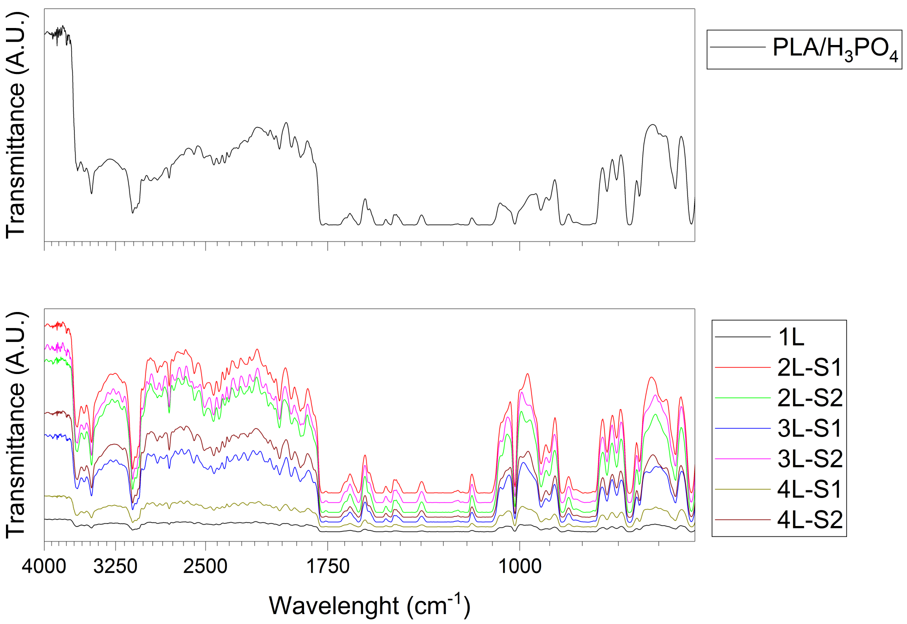

FIGURE B.1: FTIR spectrum of the thermoelectric films.

Bibliography

[1] A. Das, S. C. M. Sharma, and B. K. Ratha, "Chapter 1 - The New Era of Smart Cities, From the Perspective of the Internet of Things," in *Smart Cities Cybersecurity and Privacy*, D. B. Rawat and K. Z. Ghafoor, Eds. Elsevier, 2019, pp. 1–9. [Online]. Available: https://doi.org/10.1016/B978-0-12-815032-0.00001-9

[2] S. Li, L. D. Xu, and S. Zhao, "5G Internet of Things: A survey," *Journal of Industrial Information Integration*, vol. 10, pp. 1–9, 2018. [Online]. Available: https://doi.org/10.1016/j.jii.2018.01.005

[3] F. Guo, F. R. Yu, H. Zhang, X. Li, H. Ji, and V. C. M. Leung, "Enabling Massive IoT Toward 6G: A Comprehensive Survey," *IEEE Internet of Things Journal*, vol. 8, no. 15, pp. 11 891–11 915, 2021. [Online]. Available: https://doi.org/10.1109/JIOT.2021.3063686

[4] M. Aboubakar, M. Kellil, and P. Roux, "A review of IoT network management: Current status and perspectives," *Journal of King Saud University - Computer and Information Sciences*, vol. 34, no. 7, pp. 4163–4176, 2022. [Online]. Available: https://doi.org/10.1016/j.jksuci.2021.03.006

[5] A. Kirimtat, O. Krejcar, A. Kertesz, and M. F. Tasgetiren, "Future Trends and Current State of Smart City Concepts: A Survey," *IEEE Access*, vol. 8, pp. 86 448–86 467, 2020. [Online]. Available: https://doi.org/10.1109/ACCESS.2020.2992441

[6] P. Bellini, P. Nesi, and G. Pantaleo, "IoT-Enabled Smart Cities: A Review of Concepts, Frameworks and Key Technologies," *Applied Sciences*, vol. 12, no. 3, 2022. [Online]. Available: https://doi.org/10.3390/app12031607

[7] M. Soori, B. Arezoo, and R. Dastres, "Internet of things for smart factories in industry 4.0, a review," *Internet of Things and Cyber-Physical Systems*, vol. 3, pp. 192–204, 2023. [Online]. Available: https://doi.org/10.1016/j.iotcps.2023.04.006

[8] S. Aheleroff, X. Xu, Y. Lu, M. Aristizabal, J. Pablo Velásquez, B. Joa, and Y. Valencia, “IoT-enabled smart appliances under industry 4.0: A case study,” *Advanced Engineering Informatics*, vol. 43, p. 101043, 2020. [Online]. Available: https://doi.org/10.1016/j.aei.2020.101043

[9] A. Laghari, K. Wu, R. Laghari, M. Ali, and A. Ayub Khan, “A Review and State of Art of Internet of Things (IoT),” *Archives of Computational Methods in Engineering*, vol. 29, pp. 1395–1413, 2022. [Online]. Available: https://doi.org/10.1007/s11831-021-09622-6

[10] C. Jiang, X. Li, S. W. M. Lian, Y. Ying, J. S. Ho, and J. Ping, “Wireless Technologies for Energy Harvesting and Transmission for Ambient Self-Powered Systems,” *ACS Nano*, vol. 15, no. 6, pp. 9328–9354, 2021. [Online]. Available: https://doi.org/10.1021/acsnano.1c02819

[11] M. Haras and T. Skotnicki, “Thermoelectricity for IoT – A review,” *Nano Energy*, vol. 54, pp. 461–476, 2018. [Online]. Available: https://doi.org/10.1016/j.nanoen.2018.10.013

[12] O. Martínez Rosabal, O. L. A. López, D. E. Pérez, M. Shehab, H. Hilleshein, and H. Alves, “Minimization of the Worst Case Average Energy Consumption in UAV-Assisted IoT Networks,” *IEEE Internet of Things Journal*, vol. 9, no. 17, pp. 15 827–15 838, 2022. [Online]. Available: https://doi.org/10.1109/JIOT.2022.3150419

[13] H. Elahi, K. Munir, M. Eugeni, S. Atek, and P. Gaudenzi, “Energy Harvesting towards Self-Powered IoT Devices,” *Energies*, vol. 13, no. 21, 2020. [Online]. Available: https://doi.org/10.3390/en13215528

[14] Z. Jiang, X. Tan, and Y. Huang, “Piezoelectric effect enhanced photocatalysis in environmental remediation: State-of-the-art techniques and future scenarios,” *Science of The Total Environment*, vol. 806, p. 150924, 2022. [Online]. Available: https://doi.org/10.1016/j.scitotenv.2021.150924

[15] Q. Shi, Z. Sun, Z. Zhang, and C. Lee, “Triboelectric Nanogenerators and Hybridized Systems for Enabling Next-Generation IoT Applications,” *Research*, vol. 2021, 2021. [Online]. Available: https://doi.org/10.34133/2021/6849171

[16] M. P. dos Santos, D. A. Vieira, Y. P. M. Rodriguez, C. P. d. Souza, T. O. d. Moraes, and R. C. S. Freire, "Energy harvesting using magnetic induction considering different core materials," *2014 IEEE International Instrumentation and Measurement Technology Conference (I2MTC) Proceedings*, pp. 942–944, 2014. [Online]. Available: https://doi.org/10.1109/I2MTC.2014.6860881

[17] M. Hamid Elsheikh, D. A. Shnawah, M. F. M. Sabri, S. B. M. Said, M. Haji Hassan, M. B. Ali Bashir, and M. Mohamad, "A review on thermoelectric renewable energy: Principle parameters that affect their performance," *Renewable and Sustainable Energy Reviews*, vol. 30, pp. 337–355, 2014. [Online]. Available: https://doi.org/10.1016/j.rser.2013.10.027

[18] L. Sucupira and J. Castro-Gomes, "Review of Energy Harvesting for Buildings Based on Solar Energy and Thermal Materials," *CivilEng*, vol. 2, no. 4, pp. 852–873, 2021. [Online]. Available: https://doi.org/10.3390/civileng2040046

[19] M. Papapetrou, G. Kosmadakis, A. Cipollina, U. La Commare, and G. Micale, "Industrial waste heat: Estimation of the technically available resource in the EU per industrial sector, temperature level and country," *Applied Thermal Engineering*, vol. 138, pp. 207–216, 2018. [Online]. Available: https://doi.org/10.1016/j.applthermaleng.2018.04.043

[20] Y. Lin, C. H. Chong, L. Ma, Z. Li, and W. Ni, "Quantification of waste heat potential in China: A top-down Societal Waste Heat Accounting Model," *Energy*, vol. 261, p. 125194, 2022. [Online]. Available: https://doi.org/10.1016/j.energy.2022.125194

[21] H. Jouhara, A. Żabnieńska Góra, N. Khordehgah, Q. Doraghi, L. Ahmad, L. Norman, B. Axcell, L. Wrobel, and S. Dai, "Thermoelectric generator (TEG) technologies and applications," *International Journal of Thermofluids*, vol. 9, p. 100063, 2021. [Online]. Available: https://doi.org/10.1016/j.ijft.2021.100063

[22] F. Tohidi, S. Ghazanfari Holagh, and A. Chitsaz, "Thermoelectric Generators: A comprehensive review of characteristics and applications," *Applied Thermal Engineering*, vol. 201, p. 117793, 2022. [Online]. Available: https://doi.org/10.1016/j.applthermaleng.2021.117793

[23] J. B. Sousa, J. O. Ventura, A. Pereira, and J. P. Araújo, "Chapter 8 - Thermal and thermoelectrical measurements," in *Transport Phenomena in Micro- and Nanoscale*

Functional Materials and Devices, ser. Micro and Nano Technologies, J. B. Sousa, J. O. Ventura, and A. Pereira, Eds. William Andrew Publishing, 2021, pp. 209–251. [Online]. Available: https://doi.org/10.1016/B978-0-323-46097-2.00001-X

[24] Z. Fan, Y. Zhang, L. Pan, J. Ouyang, and Q. Zhang, "Recent developments in flexible thermoelectrics: From materials to devices," *Renewable and Sustainable Energy Reviews*, vol. 137, p. 110448, 2021. [Online]. Available: https://doi.org/10.1016/j.rser.2020.110448

[25] D. Beretta, N. Neophytou, J. M. Hodges, M. G. Kanatzidis, D. Narducci, M. Martin-Gonzalez, M. Beekman, B. Balke, G. Cerretti, W. Tremel, A. Zevalkink, A. I. Hofmann, C. Müller, B. Dörling, M. Campoy-Quiles, and M. Caironi, "Thermoelectrics: From history, a window to the future," *Materials Science and Engineering: R: Reports*, vol. 138, p. 100501, 2019. [Online]. Available: https://doi.org/10.1016/j.mser.2018.09.001

[26] F. Tohidi, S. Ghazanfari Holagh, and A. Chitsaz, "Thermoelectric Generators: A comprehensive review of characteristics and applications," *Applied Thermal Engineering*, vol. 201, p. 117793, 11 2021. [Online]. Available: https://doi.org/10.1016/j.applthermaleng.2021.117793

[27] D. Champier, "Thermoelectric generators: A review of applications," *Energy Conversion and Management*, vol. 140, pp. 167–181, 2017. [Online]. Available: https://doi.org/10.1016/j.enconman.2017.02.070

[28] C. R. Rodrigues, T. Machado, A. L. Pires, B. Chaves, F. S. Carpinteiro, and A. M. Pereira, "Recovery of thermal energy released in the composting process and their conversion into electricity utilizing thermoelectric generators," *Applied Thermal Engineering*, vol. 138, pp. 319–324, 2018. [Online]. Available: https://doi.org/10.1016/j.applthermaleng.2018.04.046

[29] H. Khalil and H. Hassan, "Enhancement of waste heat recovery from vertical chimney via thermoelectric generators by heat spreader," *Process Safety and Environmental Protection*, vol. 140, pp. 314–329, 2020. [Online]. Available: https://doi.org/10.1016/j.psep.2020.05.023

[30] P. Alegria, L. Catalan, M. Araiz, A. Rodriguez, and D. Astrain, "Experimental development of a novel thermoelectric generator without moving parts to harness

shallow hot dry rock fields," *Applied Thermal Engineering*, vol. 200, p. 117619, 2022. [Online]. Available: https://doi.org/10.1016/j.applthermaleng.2021.117619

[31] K. T. Park, J. Choi, B. Lee, Y. Ko, K. Jo, Y. M. Lee, J. A. Lim, C. R. Park, and H. Kim, "High-performance thermoelectric bracelet based on carbon nanotube ink printed directly onto a flexible cable," *J. Mater. Chem. A*, vol. 6, pp. 19 727–19 734, 2018. [Online]. Available: http://doi.org/10.1039/C8TA08170K

[32] N. V. Burnete, F. Mariasiu, C. Depcik, I. Barabas, and D. Moldovanu, "Review of thermoelectric generation for internal combustion engine waste heat recovery," *Progress in Energy and Combustion Science*, vol. 91, p. 101009, 2022. [Online]. Available: https://doi.org/10.1016/j.pecs.2022.101009

[33] M. Sadi and M. Farzaneh-Gord, "Introduction of Annular Vortex Tube and experimental comparison with Ranque–Hilsch Vortex Tube," *International Journal of Refrigeration*, vol. 46, pp. 142–151, 2014. [Online]. Available: https://doi.org/10.1016/j.ijrefrig.2014.07.004

[34] T. Dutta, K. Sinhamahapatra, and S. Bandyopadhyay, "Experimental and numerical investigation of energy separation in counterflow and uniflow vortex tubes," *International Journal of Refrigeration*, vol. 123, pp. 9–22, 2021. [Online]. Available: https://doi.org/10.1016/j.ijrefrig.2020.11.013

[35] Vortec. Vortex Tube Short Course. [Online]. Available: https://www.vortec.com/en-us/vortex-tube-short-course

[36] T. Karthikeya Sharma, G. Amba Prasad Rao, and K. Madhu Murthy, "Numerical Analysis of a Vortex Tube: A Review," *Arch Computat Methods Eng*, vol. 24, pp. 251–280, 2017. [Online]. Available: https://doi.org/10.1007/s11831-016-9166-3

[37] Vortec. Vortex tube - 208-11-H. [Online]. Available: https://www.vortec.com/en-us/vortex-tubes/208-11-h

[38] S.-J. Park, E.-J. Lee, and S.-H. Kwon, "Influence of Surface Treatment of Polyimide Film on Adhesion Enhancement between Polyimide and Metal Films," *Bulletin of the Korean Chemical Society*, vol. 28, 02 2007. [Online]. Available: https://doi.org/10.5012/bkcs.2007.28.2.188

[39] Y. Wang, M. Hong, W.-D. Liu, X.-L. Shi, S.-D. Xu, Q. Sun, H. Gao, S. Lu, J. Zou, and Z.-G. Chen, "$Bi_{0.5}Sb_{1.5}Te_3$/PEDOT:PSS-based flexible thermoelectric film and device," *Chemical Engineering Journal*, vol. 397, p. 125360, 2020. [Online]. Available: https://doi.org/10.1016/j.cej.2020.125360

[40] A. L. Pires, I. F. Cruz, J. Silva, G. N. P. Oliveira, S. Ferreira-Teixeira, A. M. L. Lopes, J. P. Araújo, J. Fonseca, C. Pereira, and A. M. Pereira, "Printed Flexible μ-Thermoelectric Device Based on Hybrid Bi_2Te_3/PVA Composites," *ACS Applied Materials & Interfaces*, vol. 11, no. 9, pp. 8969–8981, 2019. [Online]. Available: https://doi.org/10.1021/acsami.8b18081

[41] M. J. Mandou, *Fundamentals of Microfabrication and Nanotechnology - Volume II*. Taylor and Francis Group, 2012.

[42] Z. Cao, E. Koukharenko, M. Tudor, R. Torah, and S. Beeby, "Flexible screen printed thermoelectric generator with enhanced processes and materials," *Sensors and Actuators A: Physical*, vol. 238, pp. 196–206, 2016. [Online]. Available: https://doi.org/10.1016/j.sna.2015.12.016

[43] S. Wang, Q. Wang, J. Liu, Z. Cheng, D. Si, and B. Geng, "Kinetic manipulation of the morphology evolution of $FePO_4$ microcrystals: from rugbies to porous microspheres," *CrystEngComm*, vol. 11, pp. 2510–2515, 2009. [Online]. Available: http://doi.org/10.1039/B907979N

[44] Z. Zhang and S. Wang, *Novel Organic Polymer Composite-Based Thermoelectrics*. Cham: Springer International Publishing, 2021, pp. 123–153. [Online]. Available: https://doi.org/10.1007/978-3-030-45862-1_5

[45] M. Massetti, F. Jiao, A. J. Ferguson, D. Zhao, K. Wijeratne, A. Würger, J. L. Blackburn, X. Crispin, and S. Fabiano, "Unconventional Thermoelectric Materials for Energy Harvesting and Sensing Applications," *Chemical Reviews*, vol. 121, no. 20, pp. 12 465–12 547, 2021, pMID: 34702037. [Online]. Available: https://doi.org/10.1021/acs.chemrev.1c00218

[46] S. Alipoori, M. Torkzadeh, S. Mazinani, S. H. Aboutalebi, and F. Sharif, "Performance-tuning of PVA-based gel electrolytes by acid/PVA ratio and PVA molecular weight," *SN Applied Sciences*, vol. 3, 03 2021. [Online]. Available: http://doi.org/10.1007/s42452-021-04182-7